

**QUANTIFICATION OF SCATTERING
FORCES IN A MICROFLUIDIC CHANNEL**

James White

Bachelor of Engineering
Mechatronic Engineering Major



Department of Electronic Engineering
Macquarie University

November 7, 2016

Supervisor: Dr. David W. Inglis



ACKNOWLEDGMENTS

Thank you Dr. David Inglis, for your support and motivation throughout my engineering degree. This thesis was realised by your understanding and approachability. I have enjoyed this experience and hope we will continue to work together.


Thank you Mathieu, Shilun, Carlo, Lianmei, Rong and Taylor for your contributions to this thesis and thank you to my Family and Friends for your irrevocable love.



STATEMENT OF CANDIDATE

I, (James White), declare that this report, submitted as part of the requirement for the award of Bachelor of Engineering in the Department of Electronic Engineering, Macquarie University, is entirely my own work unless otherwise referenced or acknowledged. This document has not been submitted for qualification or assessment at any academic institution.

Student's Name: James White

Student's Signature: 

Date: 7 - November - 2016



ABSTRACT

Biological imaging will advance when fluorescent markers overcome the limitations of toxicity and photo instability. Recent work by Brown [31] indicates that fluorescent nanodiamonds avoid these limitations, as the carbon composition of the diamond removes toxicity and the embedding of defects in the diamond lattice increases photo stability. The current limitation to the use of nanodiamonds in imaging applications is the brightness variations from particle-to-particle [14]. A new project at Macquarie University aims to improve the brightness uniformity of nanodiamond materials using optical forces to sort particles by brightness. This thesis targets the first aim of the recently funded Macquarie project (DP170103010) which is to quantify the effect of scattering forces on nanomaterials. Fulfilling this aim required the development of a microfluidic device that was capable of observing nanomaterials and enabling laser access. Particles in the channels of the developed devices were observed under the impact of a high powered laser and video data was analysed to track and map the trajectory of each particle. The experiment did not observe an optical force as the particles were not significantly impacted by the path of the laser. We believe that insufficient laser power was entering the channel due to the shallow height of the optical access. Future work on this project will require additional control of the laser setup and a redesign of the devices' optical accessibility.



Contents

Acknowledgments	iii
Abstract	vii
Table of Contents	ix
List of Figures	xiii
List of Tables	xvii
1 Introduction	1
1.1 Document Structure	2
1.2 Thesis Process	2
1.3 Budgeting and Scheduling	3
1.3.1 Budgeting	3
1.3.2 Time Schedule	4
2 Background and Theory	5
2.1 Nanodiamonds	5
2.1.1 Techniques used to manufacture Nanodiamonds	5
2.1.2 Fluorescent Nanodiamonds	6
2.1.3 Properties of Nanodiamonds	7
2.2 Optical Physics	7
2.2.1 Optical Theory	7
2.2.2 Quantisation of Light	10
2.2.3 Optical Forces	11
2.2.4 Selective sorting theory	14
2.3 Microfluidics	15
2.3.1 Fluid Mechanics	15
2.3.2 Suspended Particle Interactions	16
2.3.3 Microfluidic Device Fabrication	17
2.4 Optical Microscopy	20
2.4.1 Microscopy Terminology	20
2.4.2 scale=	22

2.4.3	Epifluorescence Microscopy	23
2.4.4	Dark Field Microscopy	24
2.5	Particle Tracking	25
3	Microfluidic Device Fabrication	27
3.1	Design of the Microfluidic Device	27
3.2	Process of Fabrication	30
3.2.1	Photolithography	30
3.2.2	Soft Lithography	32
3.2.3	Fabrication of an Optical Window	33
3.3	Process Revisions	35
3.3.1	Channel Height Reduction	35
3.3.2	UV Exposure Dosage	36
3.4	Chapter Summary	37
4	CSIRO Laser experiment	39
4.1	Optical Configuration	40
4.2	Components of the optical setup	41
4.3	Microscope Configuration	43
4.4	Components of the microscope setup	44
4.5	Video Results	45
4.6	Process Revisions	46
4.6.1	Fluid Intake and diffusion	46
4.6.2	Device Mount	46
4.7	Discussion of the Laser Experiment	47
4.8	Chapter Summary	47
5	Processing and Analysis of Laser Experiment	49
5.1	Theoretical Analysis	49
5.1.1	Experimental Expectations	50
5.1.2	Optical Force Equations	50
5.1.3	Selected Variables of the Experiment	51
5.1.4	Optical Force Approximation	52
5.1.5	Theoretical Particle Behaviour	52
5.2	Particle Tracking	52
5.2.1	Methodology	53
5.2.2	Results	55
5.3	Discussion of Analysis	57
5.4	Chapter Summary	59
6	Conclusions and Future Work	61
7	Abbreviations	65

A Calculations and Plots	67
A.1 Matlab	67
A.1.1 Matlab to generate the Vector Plot	67
A.1.2 Matlab to generate the Particle Trajectory Plots	68
A.2 Vector Calculation	69
Bibliography	69



List of Figures

2.1	Representation of a Silicon-Vacancy Centre embedded in the lattice of a nanodiamond. The grey spheres represent carbon atoms, the green sphere represents a Silicon atom that has been sandwiched between two less visible vacancies, the orange spheres and links show the bonding of the SiV to the lattice of the nanodiamond [40].	6
2.2	Illustration of the laws of reflection and refraction. The image creates 2 paths from a single incident ray. The splitting of light into reflected and refracted parts often occurs at boundaries where the properties of reflectance and transparency are present (PDMS, glass). The angle of the incident ray is equal to the angle of the refracted ray. The incident ray experiences an increase in refractive index ($n_1 < n_2$) beyond the boundary, this causes the refracted angle to decrease (shift towards the normal). . . .	8
2.3	Illustrates the concept of TIR. The critical angle is defined as θ_2 , at this angle the light is refracted along the boundary. θ_1 is smaller than the critical angle and refracted into the material. θ_3 is larger than the critical angle reflecting the incident light off the material.	9
2.4	This is a free body diagram of the forces experienced by a nanoparticle that are absorbing and emitting photons. The left particle shows the effect of a directed absorption, as photons travel from below the particle causing an upward force as a result of absorption. The right particle shows the isotropic emission, photons are emitted in all directions causing a negligible net kick (as the random direction of emission generates a net force of 0N over time).	11
2.5	This uses a similar setup to the Neild group that used scattering forces to sort particles by size [28]. This figure deconstructs the selective sorting method into resonant and non-resonant forces. All forces are applied across the axis of the channel width. The net force is in the direction of resonant scattering force, as this direction applies a resonant and non-resonant scattering force to selectively impact FND defects.	14
2.6	The process of photolithography for the microfabrication of detailed structures. This image illustrates the non-baking stages of photolithography, building a structure on a silicon wafer.	18

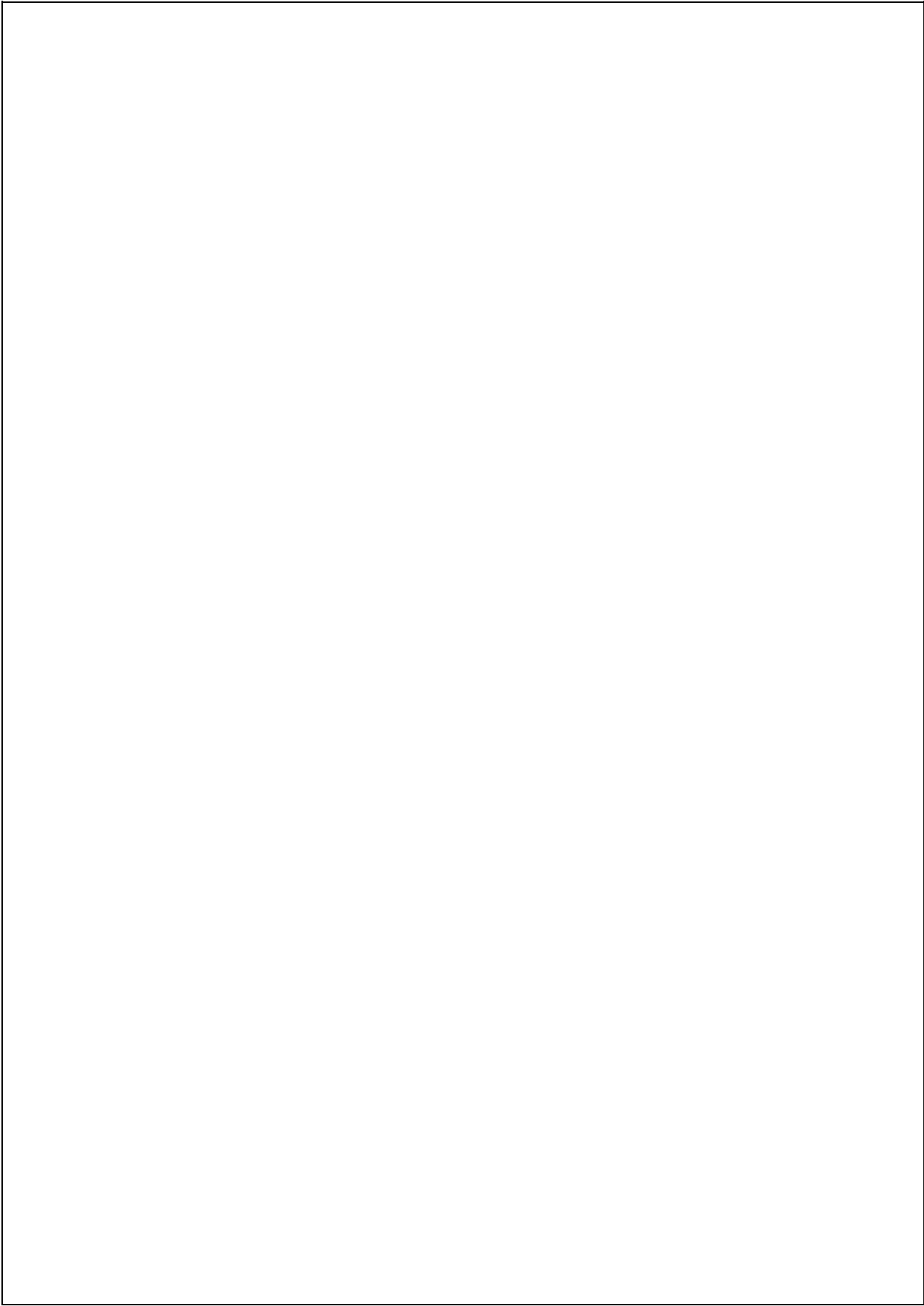
2.7	Illustration of the process of soft lithography [9]. 1. The master mould is created by photolithography. 2. The PDMS is poured over the mould. 3. The PDMS is peeled from the mould 4. The Inlets are punched into the PDMS peel 5. The plasma treatment prepares the PDMS and flat surface for bonding. 6. The two surfaces are sandwiched.	19
2.8	This image shows the major components of an inverted microscope.	20
2.9	Illustration of the half angle θ of an inverted microscopes numerical aperture.	21
2.10	A. (left) This is a schematic of the bright field configuration. The light source is collimated by a condenser and focused to a point on the specimen. The light captures a silhouetted image of the specimens obstructions before being magnified by the objective. The objectives image is reflected and refocused by the eyepiece. B. (right) This is a bright field image of fluorescent beads in a microfluidic channel that was fabricated during this thesis. The beaded solution is spreading from the centre as the advancing meniscus can be seen in the thick edges to the left of the image.	22
2.11	A. (left) The sample is excited by the light of the blue line, this light travels from the source through the filter cube and objective before hitting the sample. The emission light (the green line) travels back through the objective before being redirected by the filter cube towards the eyepiece. B. (right) An image of 500 nm YG fluorescent beads inside a microfluidic device	23
2.12	A. (left) illustrates a block diagram of the dark field microscopy setup that was used in the optical experiment of this thesis. The laser was focused by a spherical lens to direct the beam into the microfluidic device, the light scattered off particles and the scattered light was captured by the objective. B. (right) is a dark field image of particles inside the microfluidic channel of this thesis.	24
2.13	Example of the Particle Detection process, the left frame includes a sample of particles with some small, large, dull and conjoint particles. The right frame shows the selections of the detection step. The detections selects green particles but rejects the red particles.	25
2.14	A. Illustrates the expected displacement radius for a set of detected particles. B. Illustrates the linking of particles inside the expected displacement radius. C. Defines the particle separation as Δ	26
3.1	Schematic of the photolithographic mask that was used in the fabrication of the channel. This mask is transparent in the white areas and opaque in the black areas. The device features inlet/outlet plugs, connecting tubing and a pillared channel. The device is designed to be treated with an inlet and outlet end. The fluid flows into one pair of inlets along the channel length before flowing out of a pair of outlets.	28

3.2	The devices of this thesis used half of the channel, allowing 2 devices to be fabricated from a single PDMS peel. The device was assembled with the embedded PDMS bonded to a cover glass slide. The device was then reoriented to apply additional PDMS and enable optical access along the channel edge.	29
3.3	The 3 crystallising dishes used to develop the SU-8 structures of the exposed wafer. The first dish (left) was used to catch the run off of the SU-8 developer, the second dish was used as a clean bath of SU-8 developer and the third dish (right) was used to catch the run off of the rinsing isopropanol.	31
3.4	The excess PDMS was removed using a blade to along the edge of the cover glass (dotted line).	33
3.5	A bulldog clip holds the device and slide at a perpendicular to the base surface. This configuration is used to set the PDMS of the optical window inside the oven.	33
3.6	Image of the microfluidic channel with optical side accesss, taken through the side access to capture the cross section of the 6 μm channel.	34
3.7	Image of the microfluidic channel with optical side access shows the top view of the same portion of the device.	34
3.8	A. (left) Image of the 6 μm channel produces a focused image with a clear contrast between the uniform particles and the channel features. B. (right) Image of the 30 μm channel produces a clouded image with extreme difference in the size and intensity of the recorded particles.	35
3.9	Exposure lengths plotted against the accuracy of the resulting SU8 structures. The red line highlights the average error of feature size against the length of exposure. The blue line plots the average error of feature separation against the length of exposure.	36
4.1	The setup was installed on an optical table that featured a grid of tapped holes that eased component installation. The optical system started at the Laser diode controllers that defined the behaviour of the laser diode. The mounted laser diode emitted a laser onto 4 mirrors before being captured by a fibre launcher. Fibre transmitted the light through a manual polarisation controller. A spatial filter re-emitted the light from the fibre as a Gaussian beam. The Gaussian beam was then reflected towards a spherical lens that focused the laser to a point inside the channel of the microfluidic device. The resulting image was input to the computer via a CCD camera. A schematic of the microscope setup is provided in figure 4.2 with a description of the microscopes configuration and components provided in sections 4.5 and 4.6.	40

4.2	The microscope placed an objective beneath the channel of the microfluidic device. The image produced by the objective was reflected by the filter cube towards a pair of mirrors (figure 4.1). These mirrors passed the image towards the lens of a computer connected CCD camera. The bright field setup illuminated the device with a halogen lamp (mounted above the stage). To perform dark field microscopy, the lamp was disconnected and the light that scattered off disturbances was captured by the objective. . . .	43
4.3	A (top left) a bright field image of the channel under a high laser power, stuck particles and a single pillar are observable. B (top right) an image that combines the outputs of bright field and dark field microscopy to overlay the path of the laser onto a bright field image of the channel. C (bottom left) a dark field image that was taken with a low powered objective. D (bottom right) an image of dark field microscopy using a high powered objective.	45
5.1	This is a dark field image of the lasers path overlaid with a vector plot of the optical forces related to a $40\text{ }\mu\text{m}$ beam waist ($2w_0$). The force vectors length corresponds with the magnitude of the force and the orientation of the vector arrow defines the direction of the force.	53
5.2	A. (top) Plots the trajectory of the particles relative to the 10 mW beam path (the pink box is equivalent to a $40\text{ }\mu\text{m}$ beam waist). B. (bottom) Plots the trajectory of each particle under a low powered laser from a common origin. The common origin figure shows the diffusion of the particle moving right to left under the capillary action.	55
5.3	A. (top) Plots the trajectory of the particles relative to the 70 mW beam path (the pink box is equivalent to a $40\text{ }\mu\text{m}$ beam waist). B. (bottom) Plots the trajectory of each particle under a high powered laser from a common origin. These figures capture a larger sample of particles, highlighting the right to left effect of the capillary action.	56
5.4	This image illustrates the significant drop off in laser power that was attributed to the shallow height of the channel and the conditions for total internal reflection. The laser travels from the left and rays that are not incident on the channel wall are reflected due to total internal reflection. This figure uses the refractive indices of each material to highlight the the conditions for TIR.	57
5.5	This image highlights the control requirement for the system, as the gaussian distribution shows significant drop offs in intensity away from the normal. The beam waist ($2w_0$) is equal to $40\text{ }\mu\text{m}$ and the laser propagates in the direction of positive z	58

List of Tables

1.1	Cost of fabrication and experimental procedures	3
1.2	Gantt chart outlining the schedule of this thesis	4
2.1	Flow Regime - Reynolds number relationship	15
2.2	Objective Specifications	21
3.1	Dimensions of the Channel	28
3.2	Plasma Settings for Cleaning	30
3.3	Plasma Settings for Bonding	32
3.4	UV Lamp intensity over time	37
4.1	Specifications of the microscopes objective	44
5.1	Parameters of the laser experiment	51
5.2	Expected Particle Velocity based on Optical Force Approximations.	54
A.1	Approximated Force Vectors for a 40 μm beam waist	69



Chapter 1

Introduction

Engineering is the application of logic and scientific understanding to problems. Engineers pursue progress and attempt to resolve limitations using a process of design. Microscopic sciences are frequently limited by resolution, as the instrument and user face a condition where they are unable to observe the smallest features. An example of this resolution limit is the inability to directly observe the molecular interactions within cellular processes, that is considered a major frontier to understanding biological science [19]. The diffraction limit represents an enduring resolution constraint that results from using visible light to image specimens [23]. Biological imaging (including recently developed super resolution techniques) are limited by their dependence on fluorescent markers that currently exhibit the shortfalls of toxicity and photo instability.

Many researchers around the world have successfully used fluorescent nanodiamonds (FND) as an biological imaging agent [18]. The nanodiamonds (ND) exhibit superiority to currently available markers due to their biocompatibility, photo stability, small size, and ultra-bright fluorescence [33]. The barrier to the use of FND in microscopic applications is that current methods of manufacturing and post processing produce FND materials that exhibit a high brightness non-uniformity from particle to particle. Brightness non-uniformity is a problem for molecular or sub-cellular imaging because the variations in brightness will misrepresent the concentration of labelled molecules (distorting the image).

The aim of a new project, led by Dr L. Brown (CBMS), Dr T. Volz (Physics) and Dr D. Inglis (Engineering) is to output a superior ND material that exhibits brightness uniformity. To achieve this the project will develop a novel method of brightness separation that exploits resonant optical forces to manipulate the trajectory of suspended NDs within a microfluidic channel. The projects unique method of optical manipulation and the optofluidic sorting device that the project develops, may be transferable to other applications where dielectric responses can be targeted by resonant radiation forces.

The goal of this thesis is to demonstrate a proof of concept that enables the practical implementation of the larger project. The first aim of this thesis is to develop microfluidic devices for the characterisation and separation of NDs. The second aim is to examine the impact of optical forces that result from the exposure of suspended FNDs to radiation pressures.

1.1 Document Structure

This document is structured with 6 chapters. The second chapter covers background and theory, highlighting the key ideas used in the execution of this thesis and the larger project. The following three chapters review the experimental procedures with integrated results and discussion sections: Chapter 3 outlines the methods used to create microfluidic devices, Chapter 4 reviews the experimental setup used to impact and observe the nanoparticles under radiation pressures and Chapter 5 analyses the results of the experimental procedures, modelling scientific theory against empirical results. Chapter 6 concludes the document, summarising the thesis while providing an outlook to future work on the project.

1.2 Thesis Process

A number of steps were required to observe and quantify optical forces experimentally. The first step required the fabrication of a microfluidic device that enabled the observation of nanomaterials. To complete this fabrication, photolithography was used to create a plug of the channel. Soft lithography was then used to peel the channel structures onto an elastomer. The raised elastomer was bonded to cover glass to form a microfluidic channel.

The second step of fabrication required the modification of the microfluidic device to enable laser propagation inside the device. The device was modified for optical access with additional soft lithography applied to the channel-side of the device. The construction of an optically accessible device enabled project collaboration with the Volz group. This team established an optical setup, that directed a focused laser into the channel-side of the device (propagating the laser light across the channel width). The particle displacement was recorded using magnified videos, to observe the effect of variations in applied radiation pressure.

The final step in the quantification of optical forces, required an analysis of the interaction between the particles and path of the laser. This analysis was completed with image processing and particle tracking techniques that identified the trajectory of each particle. This thesis summarises the progress of the project from conception to completion.

1.3 Budgeting and Scheduling

The large scale and extended duration of this project required effective budgeting and scheduling to ensure the realisation of the aims of this thesis.

1.3.1 Budgeting

The financial allotment for this thesis was reinvested into the Macquarie University Laboratories of E6A-218 and E7B-338, as the project's completion required the use and depletion of the laboratory's inventory during fabrication and experimental procedures. An estimate of the fabrication and experimental costs is provided in Table 1.1.

Table 1.1: Cost of fabrication and experimental procedures

Product	Total Cost \$
Silicon Wafer	50
Acetone	30
2 – Propanol	30
SU8	100
PDMS	40
Fluorescent Beads	20
Consumables*	5
Running Costs**	75
Total	300

* Consumables include blades, petri dishes, gloves and hair nets.

** Running Costs include the gas, electricity, suit cleaning and device maintenance.

The reinvestment in the laboratories will be for an equivalent exchange of value. The laboratory managers will complete a series of purchases that are required for the maintenance of the rooms inventory with a budget for reinvestment totalling \$300.

The scheduling of this thesis was dependent on submissions and task progression. The submission dates were defined by the university course, while the process of experimental progression was sequential. The requirement for laser use in this thesis introduced a need for collaboration, at this point the schedule was dependent on the availability of the Volz group. Table 1.2 outlines a Gantt chart for the path of this thesis with subheadings for bureaucracy, experimentation, analysis, documentation and submission. The x markings highlight work completed by week.

Table 1.2: Gantt chart outlining the schedule of this thesis

[illegible]

Chapter 2

Background and Theory

The Brown, Volz and Inglis project aims to optically sort a stream of nanodiamonds using the optical forces created by radiation pressures. This method of manipulation and the related sorting applications offer a range of cutting edge advancements to microscopic sciences. This section explores the fields and theories present in this thesis and explains the forces used in the conception of this project. Literature has been used to provide context and support the resident theories. This chapter has sections on Nanodiamonds (2.1), Optical physics (2.2), Microfluidics (2.3), Optical microscopy (2.4) and Particle tracking (2.5).

2.1 Nanodiamonds

Mechanical industries have exploited the properties of diamond for over a millennium. Recently, synthetic NDs have been used in optical, electronic and biological applications due to the unique qualities of their structural composition [20]. This section outlines the manufacturing techniques, properties and characteristics of FNDs. This thesis uses the superior qualities of ND imaging agents, to support the sorting application of the larger project.

2.1.1 Techniques used to manufacture Nanodiamonds

NDs are created by manufacturing processes that expose carbon materials to extreme conditions, the processes are used to break down carbon structures into nanoscale diamonds. The following list from Carlo Bradac's paper on NDs with Nitrogen Vacancies [7] outlines some techniques that are used to manufacture NDs:

- The exposure of carbon materials to high pressure/ high temperature conditions;
- The detonation of carbon based explosives;
- The deposition of a hydrocarbon gas in chamber;
- Radiation damage of a carbon material.

Mass producers such as Sigma Aldrich, use radiation damage to produce large quantities of FND [10]. The extreme conditions of the fabrication process are responsible for the photo stability of FND, as the lattice is disrupted and embedded with fluorescent defects during processing [4].

2.1.2 Fluorescent Nanodiamonds

FND are carbon materials with embedded crystallographic defects. ND defects are naturally occurring however processing and fabrication can introduce additional defects to the material [34]. Defects disrupt the regular lattice of the ND, as vacancies and elementary impurities become embedded in the structure. The defects act as fluorophores, absorbing and re-emitting light in response to a range of exciting wavelengths [43].

Colour centres are used to define fluorescent lattice defects. The Nitrogen-Vacancy (NV) centre is a well documented defect as it regularly appears in diamond structures [34]. Techniques have been developed for NV centres that can produce large quantities of highly fluorescent and uniformly sized NDs [37]. The Macquarie University project has targeted the Silicon-Vacancy (SiV) centre (figure 2.1), as it has a higher defect density and smaller particle size compared to NV centres [17]. The increased defect density is expected to amplify the separating effect of resonant optical forces while the reduced particle size will increase the ratio of fluorescent brightness to volume [25].

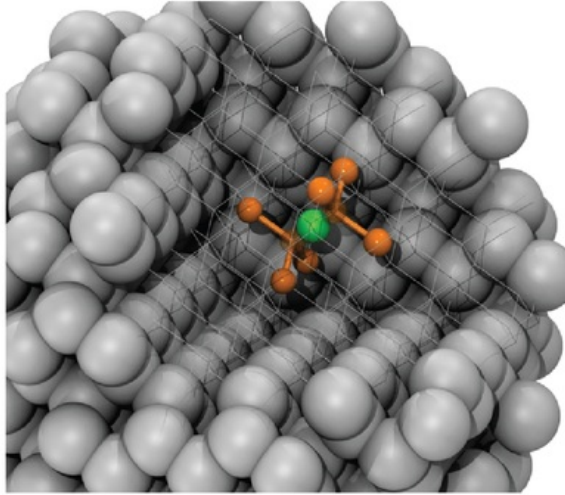


Figure 2.1: Representation of a Silicon-Vacancy Centre embedded in the lattice of a nanodiamond. The grey spheres represent carbon atoms, the green sphere represents a Silicon atom that has been sandwiched between two less visible vacancies, the orange spheres and links show the bonding of the SiV to the lattice of the nanodiamond [40].

2.1.3 Properties of Nanodiamonds

The carbon composition of nanodiamonds makes the markers highly biocompatible [39]. The exposed functional groups, large surface area and non-zero surface charge of nanodiamonds facilitate the attachment of microscopic products to the surface of the nanodiamond for delivery applications [8].

The embedding of defects into the structure of NDs overcomes the shortfalls of photo bleaching (a chemical change that inactivates molecular fluorescences) and photo blinking (a temporary and random fluorescence intermittence). FND photostability enables an extended observation of the product as a biomarker, FNDs have been observed in living tissue for over ten hours [18].

The project selected the SiV centre as the small size and short fluorescent lifetime of the ND are expected to improve the results of selective sorting (outlined in section 2.2.4). ND's with a high concentrations of SiV centres have been fabricated at a radius of 5 nm [39]. These NDs are typically spherical and supplied as a powder or liquid suspension. The 2 ns fluorescent lifetime of SiV centres is a short interval that is expected to increase the effect of resonant scattering forces. The lifetime defines the period from photon absorption to the re-emission of a photon, a reduced lifetime is advantageous as it results in an increased scattering force effect. The 700 nm wavelength of SiV centre emissions is advantageous in bioimaging applications as it can be easily distinguished from the emissions of biological materials [35].

2.2 Optical Physics

Optical physics explores the theories related to electromagnetic radiation. This section introduces the principles of geometric optics, quantum theories of light, laser operation and optical forces. An understanding of optical theory is critical for an explanation of the laser setup, the methods of observation and the analysis of results.

2.2.1 Optical Theory

To simplify optical theory, it is important to decompose the travel of light into directions of travel and stages of material interaction. The ray that travels into the material is considered the incident ray, the interacted light is considered as a reflected/refracted/diffracted ray depending on the boundary conditions. Geometrical optics use rays to resolve the propagation of light into straight lines. The simplifications of optical theory allow for the examination of boundary responses to material interactions.

Reflection

The laws of reflection and refraction are illustrated by figure 2.2. The law of reflection states that the angle of incidence θ_1 equals the angle of reflection θ_3 (equation 2.1).

$$\theta_1 = \theta_3 \quad (2.1)$$

Refraction

The law of refraction states that the angle of refraction is related to the angle of incidence by the relative indices of refraction (equation 2.2) where $n_{1,2}$ are the indices of refraction for each material and $\theta_{1,2}$ are the angles of propagation relative to a line that is perpendicular to the boundary.

$$n_2 \sin \theta_2 = n_1 \sin \theta_1 \quad (2.2)$$

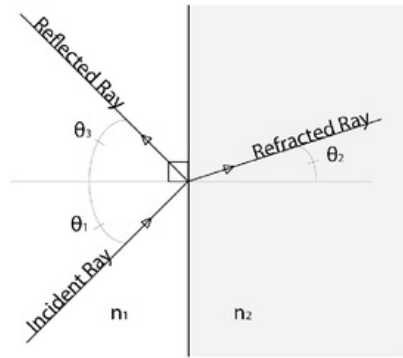


Figure 2.2: Illustration of the laws of reflection and refraction. The image creates 2 paths from a single incident ray. The splitting of light into reflected and refracted parts often occurs at boundaries where the properties of reflectance and transparency are present (PDMS, glass). The angle of the incident ray is equal to the angle of the refracted ray. The incident ray experiences an increase in refractive index ($n_1 < n_2$) beyond the boundary, this causes the refracted angle to decrease (shift towards the normal).

Diffraction

Diffraction defines the bending of light as it passes an objects edge. The amount of diffraction that occurs is dependent on the wavelength of the light relative to the size of the opening. A wavelength that is significantly smaller than the opening causes negligible diffraction, while a convergence in the relative sizes of the wavelength and opening increases the effect of diffraction.

Total Internal Reflection

Total internal reflection (TIR) is a result of refraction, as differences in refractive index change the direction of light propagation. TIR occurs as light travels from a dense material to a less dense material, the law of refraction causes the light's path to be directed away from the normal. The increased angle of refraction bends light towards the boundary plane and at a critical angle the light is directed along the boundary. Angles that are larger than the critical angle will be reflected and angles that are less than the critical angle will be refracted. These conditions are illustrated in figure 2.3.

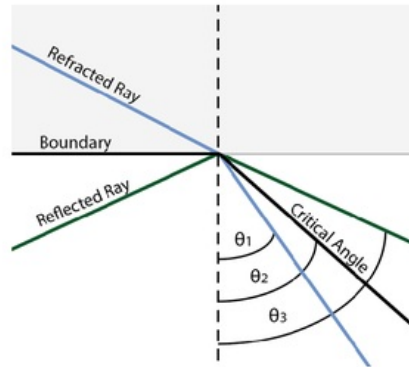


Figure 2.3: Illustrates the concept of TIR. The critical angle is defined as θ_2 , at this angle the light is refracted along the boundary. θ_1 is smaller than the critical angle and refracted into the material. θ_3 is larger than the critical angle reflecting the incident light off the material.

2.2.2 Quantisation of Light

The wave particle duality of elementary particles was famously formulated by the double slit experiment, an experiment that concluded the behaviour of light as having both particle and wave-like properties. This conclusion was extended with quantisation introducing the photon as a quantum particle of electromagnetic radiation. Photons are considered subatomic particles, that compose electromagnetic radiation as massless energy capable of transferring momentum.

The quantisation of light uses Planck's equation to fix the quantum energy of a photon to the frequency of its radiation. The quantisation of energy introduced atomic energy levels, as levels of electron excitation that require the absorption or emission of photons for a change in energy level. Interactions between photons and the energy levels of a particle are dependent on a matching of quantum energy.

The underlying principle of laser operation is the amplification of light by stimulated emission. Stimulated emission releases pairs of in-phase photons due to the interactions between photons and electron energy levels. The introduction of a foreign photon, reduces the energy state of an atom that results in the release of a photon. The original photon and released photon are amplified as the ejected photon shares a common phase and frequency to the foreign photon. The pumping of a laser system reduces the electron energy levels of the systems atoms, causing the release of photons that cause a chain reaction of stimulated emissions.

Fluorescence occurs as a high energy photon is absorbed, this photon interacts with the system to lower the energy state of the excited electron. The calming of an excited electron causes the re-emission of a photon as a result of the system returning to a lower energy state [32].

2.2.3 Optical Forces

The optical force approximations outlined in this section (2.2.3) are taken from the Y. Harada and T. Asakura paper on the scattering and gradient components of optical forces [16]. Optical traps use these forces to manipulate particles by applying attractive or repulsive forces [3]. This section reviews the theories and equations related to scattering forces, gradients forces, particle regimes, resonant scattering and selective sorting.

Scattering Forces

Scattering forces result from a particles absorption and emission of photons. The absorption kicks the particle away from the light source and the random direction of photon emission results in an isotropic kick direction. The net force of a directed absorption kick and an isotropic emission kick is in the direction of light propagation. Figure 2.3 defines a free body diagram for an absorbing and emitting particle.

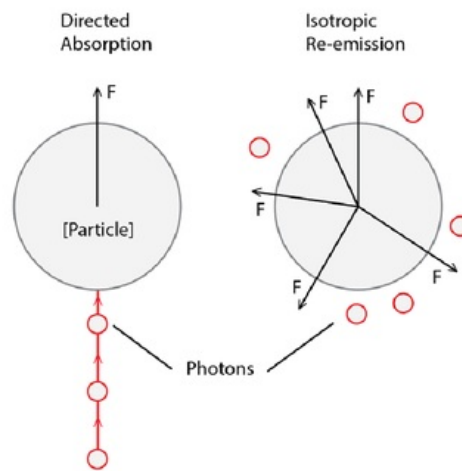


Figure 2.4: This is a free body diagram of the forces experienced by a nanoparticle that are absorbing and emitting photons. The left particle shows the effect of a directed absorption, as photons travel from below the particle causing an upward force as a result of absorption. The right particle shows the isotropic emission, photons are emitted in all directions causing a negligible net kick (as the random direction of emission generates a net force of 0N over time).

Approximation of the Scattering Force

The scattering force is a product of refraction, particle size and laser intensity. The force is derived from equation 2.3.

$$F_{scat}(r) = z \left(\frac{n_2}{c} \right) C_{scat} I(r) \quad (2.3)$$

In equation 2.3 the force acts in the direction of laser propagation z , where n_2 defines the refractive index of the environment, c denotes the speed of light, C_{scat} is the scattering cross section of the particle and $I(r)$ is the intensity distribution of light in the system. The scattering cross section is defined by equation 2.4.

$$C_{scat} = \frac{8}{3} \pi (ka)^4 a^2 \left(\frac{m^2 - 1}{m^2 + 2} \right)^2 \quad (2.4)$$

In equation 2.4, λ is the wavelength of the laser output and the wave vector (k) is given $k = 2\pi/\lambda$. a is the particle radii, m is the relative index of refraction given by $m = n_1/n_2$ where n_1 is the particles refractive index and n_2 is the environments refractive index. The intensity distribution of light in the system is defined by equation 2.5.

$$I(r) = \left(\frac{2P}{\pi w_0^2} \right) \frac{1}{1 + (2\tilde{z})^2} \exp \left[-\frac{2(\tilde{x}^2 + \tilde{y}^2)}{1 + (2\tilde{z})^2} \right] \quad (2.5)$$

In equation 2.5, P is the measured laser power, w_0 is the radius of the beams waist and $(\tilde{x}, \tilde{y}, \tilde{z})$ are the normalised spatial coordinates that are calculated from the spatial coordinates using $(x/w_0, y/w_0, z/kw_0^2)$. Using the equations for cross section and intensity results in an approximate equation for scattering force (equation 2.6).

$$F_{scat}(r) = z \left(\frac{n_2}{c} \right) \frac{8}{3} \pi (ka)^4 a^2 \left(\frac{m^2 - 1}{m^2 + 2} \right)^2 \left(\frac{2P}{\pi w_0^2} \right) \frac{1}{1 + (2\tilde{z})^2} \exp \left[-\frac{2(\tilde{x}^2 + \tilde{y}^2)}{1 + (2\tilde{z})^2} \right] \quad (2.6)$$

Gradient Forces

Optical gradient forces have a spatially dependent effect on a dipole moment. The magnitude of the force is considered a product of the systems focal length where:

- Shorter focal lengths are considered as having a steep intensity gradient that results in a large gradient force;
- Longer focal lengths are considered with a more constant gradient that results in a smaller gradient force.

The laser setup used in this document created a small intensity gradient due to the extended focal length of the beam path. Dielectric particles create dipole moments as a result of interactions between the particle and incident light [3]. The response of a dipole moment to a gradient force is dependent on the relative refractive index m . When $m > 1$ the particle travel towards the focal point seeking a higher intensity. When $m < 1$ the particle travels away from the focal point to a lower light intensity.

Approximations of the Gradient Forces

$$F_{grad,x}(r) = -\tilde{x} \frac{2\pi n_2 a^3}{c} \left(\frac{m^2 - 1}{m^2 + 2} \right) \frac{4\tilde{x}/w_0}{1 + (2\tilde{z})^2} \left(\frac{P}{\pi w_0^2} \right) \frac{1}{1 + (2\tilde{z})^2} \exp \left[-\frac{2(\tilde{x}^2 + \tilde{y}^2)}{1 + (2\tilde{z})^2} \right] \quad (2.7)$$

$$F_{grad,y}(r) = -\tilde{y} \frac{2\pi n_2 a^3}{c} \left(\frac{m^2 - 1}{m^2 + 2} \right) \frac{4\tilde{y}/w_0}{1 + (2\tilde{z})^2} \left(\frac{P}{\pi w_0^2} \right) \frac{1}{1 + (2\tilde{z})^2} \exp \left[-\frac{2(\tilde{x}^2 + \tilde{y}^2)}{1 + (2\tilde{z})^2} \right] \quad (2.8)$$

$$F_{grad,z}(r) = -\tilde{z} \frac{2\pi n_2 a^3}{c} \left(\frac{m^2 - 1}{m^2 + 2} \right) \frac{8\tilde{y}/kw_0^2}{1 + (2\tilde{z})^2} \left[1 - \frac{2(\tilde{x}^2 + \tilde{y}^2)}{1 + (2\tilde{z})^2} \right] \times \left(\frac{2P}{\pi w_0^2} \right) \frac{1}{1 + (2\tilde{z})^2} \exp \left[-\frac{2(\tilde{x}^2 + \tilde{y}^2)}{1 + (2\tilde{z})^2} \right] \quad (2.9)$$

The relative refractive index of our system caused the gradient force to act towards the focal point ($m > 1$). Equations 2.7, 2.8 and 2.9 calculate the gradient forces of each axis based on a set of normalised spatial coordinates for a system where $m > 1$.

Regimes

The Rayleigh and Mie regimes are used to characterise a particles response to radiation pressure based on an association between the incident wavelength and the radius of the particle. The Rayleigh regime defines a very small particle relative to wavelength while the Mie regime is used for particles with a radius close to the wavelength [15].

Resonant Scattering Forces

Resonance scattering uses the absorption and emissions of fluorescence to apply an additional kick to selected ND. Fluorescence causes a scattering force effect that is dependent on the quantum energy levels of the fluorescent defect and incident photons. The interaction requires that both energy levels are of a similar magnitude. The Planck equation defines the energy level of a photon as a product of the emission frequency. Therefore resonance scattering applies a resonant scattering force to a particle of a set energy level (defect density) when stimulated by an emission of an equivalent wavelength [42].

2.2.4 Selective sorting theory

The selective sorting method of the larger Macquarie University project will apply scattering forces at a perpendicular to the flow of Nanodiamonds. These forces will be supplied by laser illumination from opposite sides of the channel.

One laser will apply a non-resonant scattering force that uses laser power to act on particle size. The second laser will apply a resonant scattering that is equal in power to the size dependent non-resonant scattering force but offset to the resonant frequency of the FND. This second force will balance the effect of the non-resonant scattering force while applying a resonant scattering force due to fluorescence.

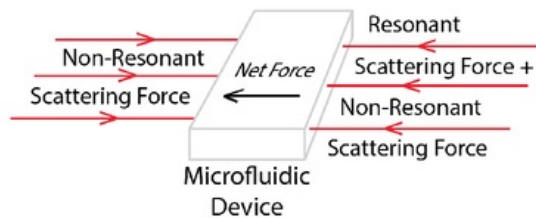


Figure 2.5: This uses a similar setup to the Neild group that used scattering forces to sort particles by size [28]. This figure deconstructs the selective sorting method into resonant and non-resonant forces. All forces are applied across the axis of the channel width. The net force is in the direction of resonant scattering force, as this direction applies a resonant and non-resonant scattering force to selectively impact FND defects.

2.3 Microfluidics

A microfluidic device was used to analyse the systems optical forces. Microfluidics create a controlled fluid flow and the devices are cheap and easy to fabricate. This section covers fluid mechanics, Brownian theory and the techniques used to fabricate microfluidic devices. This section is important as it discusses the characteristics of the devices and the expected channel conditions.

2.3.1 Fluid Mechanics

Fluid mechanics are used to examine the static and dynamic behaviour of fluid interactions. Understanding fluid mechanics is critical as the theories define the characteristics of the flow and expected interactions. Flow regimes are a cornerstone of fluid mechanics that define the conditions present in the system. The Reynolds number is often used to define these regimes, using a ratio of the systems inertial and viscous forces. The Reynolds number (Re) is defined by equation 2.10.

$$Re = \frac{\rho v L}{\mu} \quad (2.10)$$

In equation 2.10 the fluid density (ρ), flow velocity (v) and length of fluid travel (L) define the inertial force acting on the flow. The dynamic viscosity (μ) is used to define the viscous forces of the flow. Flow regimes are categorised over a range of Reynolds numbers. Table 2.1 summarises the range of Reynolds numbers for each flow regime with a brief description of the properties of each flow regime [44]

Table 2.1: Flow Regime - Reynolds number relationship

Flow Regime	Reynolds Range	Properties
Turbulent	>100	Fast and chaotic flow that results in the mixing of fluids
Laminar	10 ~ 100	Controlled flow that travels in non-mixing layers
Creeping	<1	Very slow flow that is Reversible and time independent

Microfluidic devices cause the Reynolds number to approach Laminar flow as viscosity dwarfs the channels inertia [22]. The increased viscosity of microfluidic channels, causes fluids within the system to break Bernoulli's equation for the conservation of energy as the frictional forces dissipate energy. Viscous flow is often defined by the Navier-Stokes (NS) Equation. The results of the NS equation are a set of time dependent equations for the conservation of mass, momentum and energy [11]

George Gabriel Stokes resolved the Navier-Stokes equation in 1851 to calculate the force of drag around a sphere in a viscous fluid flow (equation 2.11) [27].

$$D = 6\pi\mu Ur \quad (2.11)$$

The resulting force of drag D , was a product of the dynamic viscosity μ , flow velocity U and the radius of the sphere r . The equation is commonly used to calculate the velocity of a sphere in viscous fluid.

$$Velocity = \frac{Force}{6\pi\mu r} \quad (2.12)$$

2.3.2 Suspended Particle Interactions

This thesis required the observation of random walks in a microfluidic channel. It is important to understand that the walks of suspended particles are a result of Brownian theory. The theory states that particles are propagated by thermal energy and the random interactions between the particles and their suspending solution cause a stochastic travel [13]. The randomness of Brownian motions results in a mean displacement that is equal to zero over time, as the particles have equal probability of travelling in any direction.

Diffusion is a term used to group Brownian motions, creating a collection of stochastic walks that spread away from the centre of the particle collection. The spreading effect of diffusion causes particles to move from areas of higher concentration to areas of lower concentration. This section uses the Howards C. Berg text "Random Walks in Biology" [5] to define concepts and equations for diffusion and diffusion with drift. The introduction of an external force (F_x) such as the radiation pressure of this thesis creates a directional bias in the previously random travel of the particle. Knowledge of the external force enables the calculation of a diffusion coefficient (D) using equation 2.13.

$$f = \frac{F_x}{v_d} \quad (2.13)$$

The frictional drag coefficient f can be calculated with knowledge of the applied force (F_x) and a measurement of particles velocity (v_d). Calculation of (f) allows for an approximation of the diffusion coefficient using equation 2.14.

$$D = \frac{kT}{f} \quad (2.14)$$

2.3.3 Microfluidic Device Fabrication

The processes of photolithography and soft lithography are cornerstones of micro-fabrication. In this thesis the 2 steps of fabrication quickly create reusable microfluidic devices that are well suited to research applications. Photolithography is used to transform a mask image to minute physical structures. Soft lithography is used to create a polymer peel of the photolithographic structures, imprinting an elastomer with the details of the master mould.

Photolithography

Photolithography has a number of steps that can vary the resulting structures based on the selection of process variables. A general process is listed with a brief description of each step, figure 2.6 illustrates the process of photolithography.

Preparation: The process starts with a substrate that serves as the foundation of the process. Silicon wafers are common substrates that must be cleaned of organic material and heated before they can be used for photolithography.

Spin Coating of the photoresist: The photoresist is poured onto the silicon wafer and diffused using a spin coater to ensure that the resist has a uniform height.

Soft Baking: The coated substrate is ramped to a high temperature to remove the solvent from the photoresist.

Exposure to UV Radiation: A mask aligner is used to selectively expose the coated surface of the substrate to UV radiation. Photomasks are placed between the substrate and light source to expose regions of the photoresist to UV radiation. The resulting reaction depends on the photoresist that can be either a positive or negative resist. (Negative photoresists harden over the exposed area while Positive resists soften the exposed area)

Post Baking: The exposed photoresist is ramped to a high temperature to enhance the chemical cross linking over the harder regions.

Development: The surface of the resist is rinsed with a developer that washes away the soft regions. The resulting product has hard structures standing on the surface of the silicon substrate.

Hard Baking: This step is used to fix problems over the harder structures such as cracks and unconnected regions [1], [2].

SU-8

This thesis used GM1060 SU-8 photoresist for the process of photolithography. SU-8 is a negative photoresist that is frequently used in microfluidic fabrication as it has a high resistance to chemicals, great structural stability and low absorption coefficients. The SU8 photoresist contains a mixture composed of SU-8 monomers, organic solvents and a photo-acid generator (PAG). The solvent is removed via a soft bake after spin coating the surface and the PAG decomposes during exposure. The decomposition of PAG initialises the hardening of the exposed area through the formation of cross links [21]. Gersteltec GM1060 SU8 is capable of 6 - 50 μm layers with an aspect ratio of 1:20 [2].

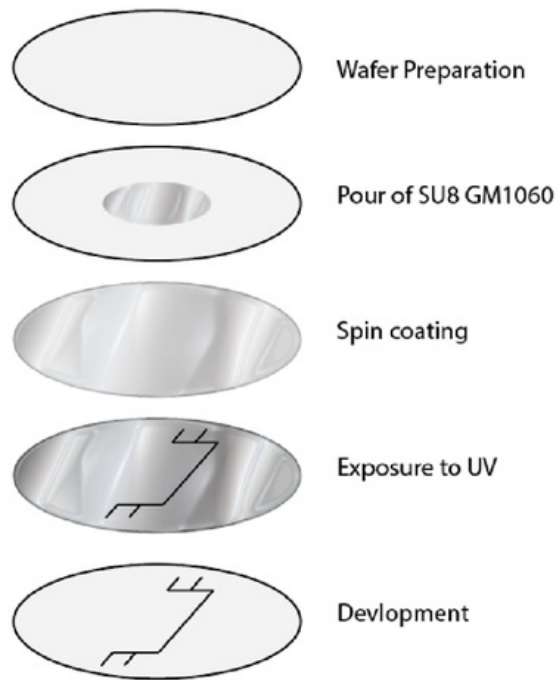


Figure 2.6: The process of photolithography for the microfabrication of detailed structures. This image illustrates the non-baking stages of photolithography, building a structure on a silicon wafer.

Soft Lithography

Soft lithography is a common extension of photolithography as it produces an elastomer with the patterned structures of the photolithographic process. The process is reliant on the elastomers ability to replicate and preserve the structures. The ability of the elastomer to then be bonded with other materials makes this fabrication technique perfect for the creation of microfluidic devices [41].

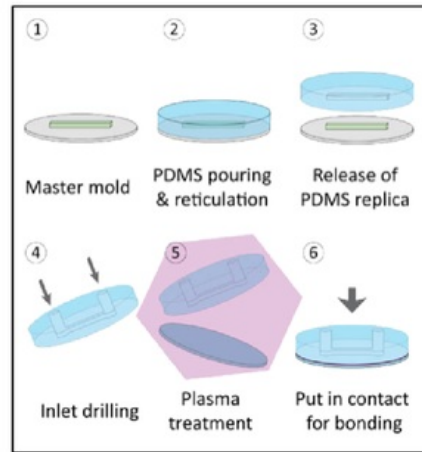


Figure 2.7: Illustration of the process of soft lithography [9]. 1. The master mould is created by photolithography. 2. The PDMS is poured over the mould. 3. The PDMS is peeled from the mould. 4. The Inlets are punched into the PDMS peel. 5. The plasma treatment prepares the PDMS and flat surface for bonding. 6. The two surfaces are sandwiched.

PDMS

In this thesis the elastomer used for soft lithography is Polydimethylsiloxane (PDMS), as the inverted meniscus and gas permeability of PDMS allow for a fidelity below $0.1 \mu\text{m}$. The PDMS used in this thesis was supplied in 2 parts, a base and curing agent that require mixing. The resulting PDMS mixture is degassed via a desiccator before being used to cast a mould. The degassed PDMS spreads to the shape of the master before setting over an extended exposure to high temperatures (2 hours at 65°C). The combination of low surface free energy and elasticity allow set PDMS to release from the master mould without damaging either surface [24].

2.4 Optical Microscopy

Methods of microscopy are a critical consideration for the observation of nanoscale interactions. Optical microscopy offers a range of techniques for the magnified observation of particles in a microfluidic channel. The microscopic techniques that were used in this thesis included fluorescent, dark field and bright field microscopy. This section reviews the common terms of microscopy before exploring the application and results of specific techniques.

2.4.1 Microscopy Terminology

Microscopes are produced with a range of configurations, however the major components of figure 2.8 are common across most setups. A light source is a requirement for optical microscopy, the sample is positioned by the stage, the objective produces an image of the sample, the eyepiece and camera observe the image and the focus varies the resolution of the image.

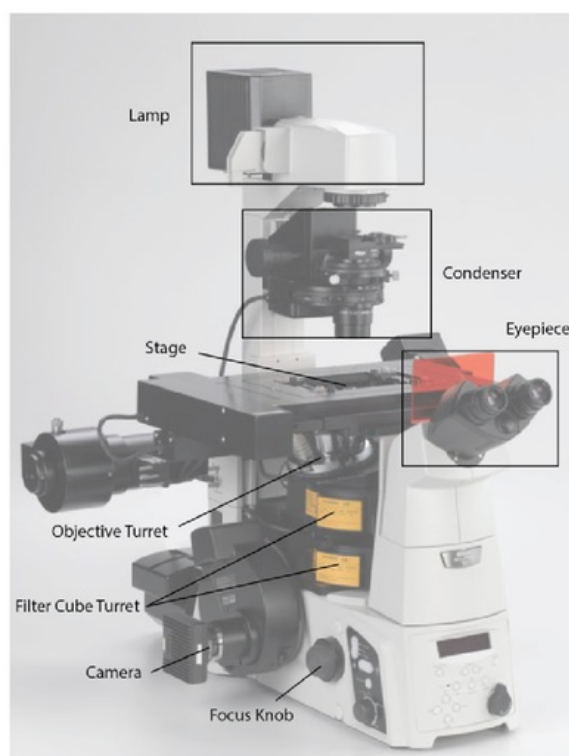


Figure 2.8: This image shows the major components of an inverted microscope.

A microscope's objective contains multiple elements that magnify the image and capture microscopic details. Table 2.2 defines the common specifications of microscope objectives.

Table 2.2: Objective Specifications

Objective Characteristic	Definition
Magnification	The lenses scaling power from object to image size.
Numerical Aperture	The light collecting ability of the lens while resolving image detail.
Coverslip Thickness	The thickness of coverslip that the objective can accommodate.
Working Distance	The distance from the edge of the lens to the in-focus sample.
Immersion Medium	Medium used to reduce image distortions due to refraction.

The Numerical Aperture (NA) of an objective is related to the index of refraction of the lens (n) and the half the angle (θ) of light that can travel through the lens by the equation $NA = n \sin \theta$ (figure 2.9 highlights the angle θ for an inverted microscope).

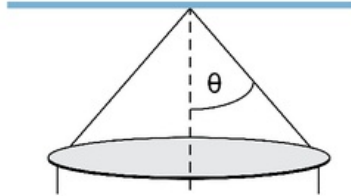


Figure 2.9: Illustration of the half angle θ of an inverted microscope's numerical aperture.

The field size (F_{size}) defines the observed sample size and the field number (F_{num}) is the number of mm observed. The two figures are related to the objective magnification (M) by the equation $F_{size} = F_{num}/M$. Depth of field defines the axial resolving power of an objective, it is measured along the optical axis between the resolved limits of the image. This figure is important when observing 3 dimensional travel as objects may travel across the objectives depth of field. Equation 2.15 defines the depth of field (Z) [26].

$$Z = \frac{\lambda n}{NA^2} \quad (2.15)$$

2.4.2 Bright Field Microscopy

Bright field microscopy illuminates an object from one side and observes the resulting image from the opposite side. Bright field is the most common form of microscopy as it is simple to set up while providing detailed images of specimens on an optical medium (figure 2.10A). The output of this technique is a silhouetted image of the object with dark objects placed against bright background (figure 2.10B). This technique requires effective sample illumination. [36].

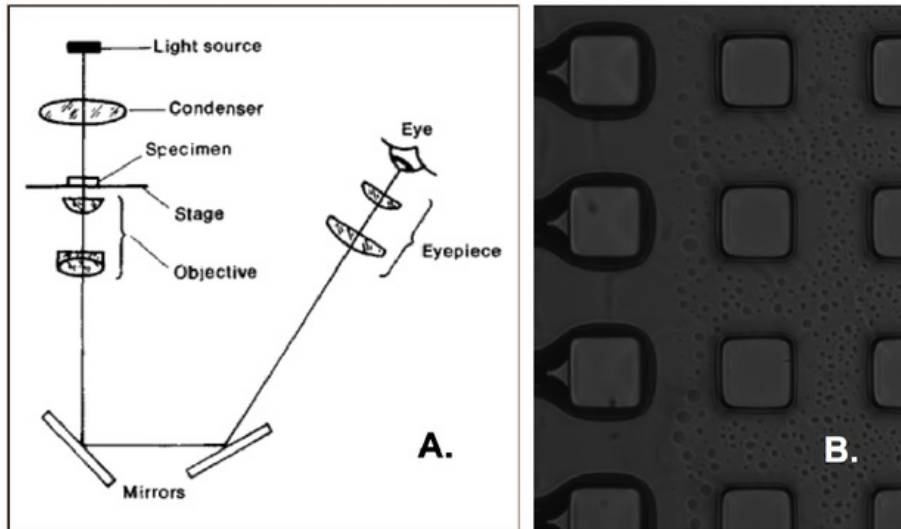


Figure 2.10: A. (left) This is a schematic of the bright field configuration. The light source is collimated by a condenser and focused to a point on the specimen. The light captures a silhouetted image of the specimens obstructions before being magnified by the objective. The objectives image is reflected and refocused by the eyepiece. B. (right) This is a bright field image of fluorescent beads in a microfluidic channel that was fabricated during this thesis. The beaded solution is spreading from the centre as the advancing meniscus can be seen in the thick edges to the left of the image.

2.4.3 Epifluorescence Microscopy

Epifluorescence microscopy images fluorescent emission against a dark background. This technique is used in biolabelling applications as the imaged particles are limited to selected emissions. The setup of a fluorescent microscope uses an LED light source to excite a sample. This light travels from the LED light source and is reflected by a filter cube towards the sample. The fluorescent emission of the sample that resulted from the excitation are returned to the filter cube. The filter cube separates the 2 paths using the stokes shift in wavelength that occurs as a result of the energy loss related to fluorescent emissions (figure 2.11A). The resulting image is directed towards the output nodes, imaging the fluorescent emissions (bright objects) against a dark background (figure 2.11B). To increase the image resolution and decrease noise effects it is important to excite the sample with a specific colour that can be differentiated from the colour of the fluorescent emission [36].

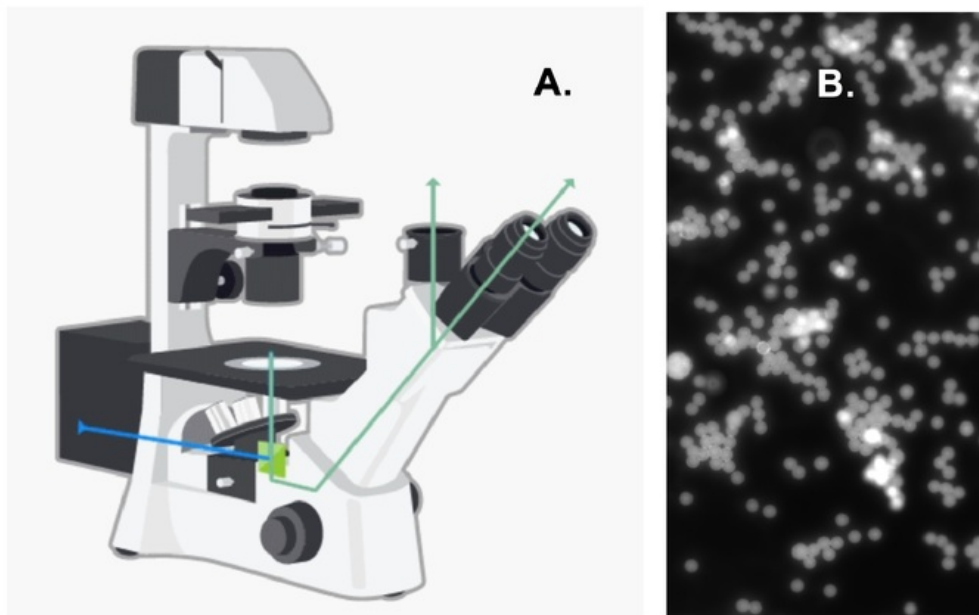


Figure 2.11: A. (left) The sample is excited by the light of the blue line, this light travels from the source through the filter cube and objective before hitting the sample. The emission light (the green line) travels back through the objective before being redirected by the filter cube towards the eyepiece. B. (right) An image of 500 nm YG fluorescent beads inside a microfluidic device

2.4.4 Dark Field Microscopy

Dark Field microscopy captures the scattering of light off disturbances, creating an image of the particles encountered by the path of illumination. The setup is designed to direct light on a path that does not enter the objective directly (figure 2.12A). A dark field setup is used in this thesis to identify the interactions between the laser and suspended particles. Dark field images have a dark background and bright features as the setup is illuminates the regions of the images corresponding to scattered light (figure 2.12B).

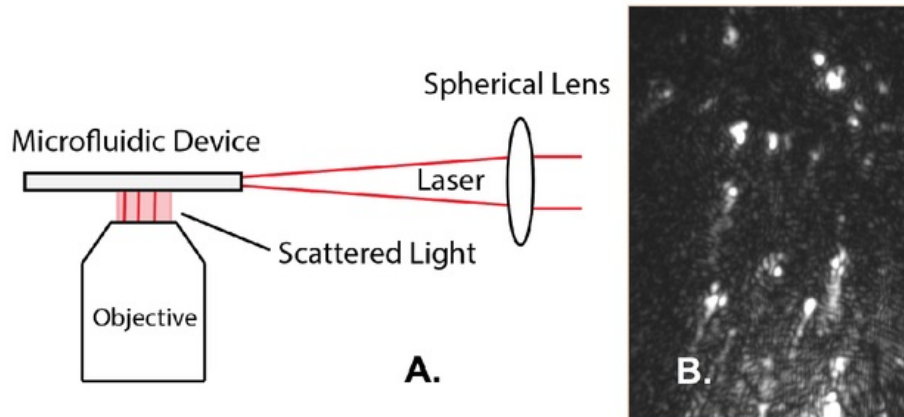


Figure 2.12: A. (left) illustrates a block diagram of the dark field microscopy setup that was used in the optical experiment of this thesis. The laser was focused by a spherical lens to direct the beam into the microfluidic device, the light scattered off particles and the scattered light was captured by the objective. B. (right) is a dark field image of particles inside the microfluidic channel of this thesis.

2.5 Particle Tracking

Particle tracking plots the motion of imaged particles over time. This thesis used particle tracking on the recorded videos to gain a set of trajectories for each particles. This was necessary as it allowed for an analysis of particle behavior inside the channel. Particle tracking requires the reiteration of particle detection and particle linking steps for each frame. These steps are applied in automated and manual particle tracking applications as both processes require particle recognition and trajectory matching to complete the tracking.

Particle Detection

The detection stage focuses on differentiating particles from non-particles. This detection is often completed with a sweep of the image that aims to identify objects within a radius range and above a brightness limit. After a particle has been detected, a particle id is applied and the coordinates are recorded.

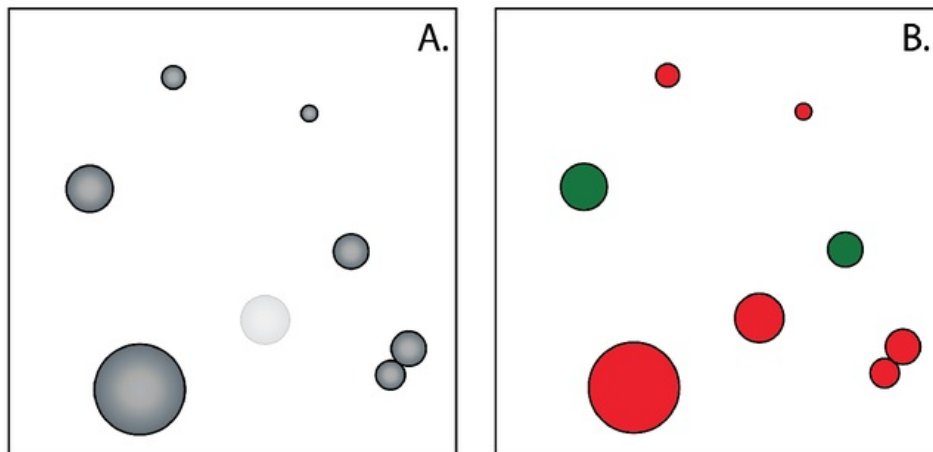


Figure 2.13: Example of the Particle Detection process, the left frame includes a sample of particles with some small, large, dull and conjoint particles. The right frame shows the selections of the detection step. The detections selects green particles but rejects the red particles.

Particle Linking

Particle linking compares successive frames in an attempt to identify the particles new position. In the new frame, a radius of expected displacement is cast around the previously detected particle locations (figure 2.14A). If a particle falls inside this radius the two locations are linked as sections of the same trajectory (figure 2.14B). Particle tracking requires a low concentration of particle, as the particle displacement (δ) must be smaller than the particle separation (Δ).

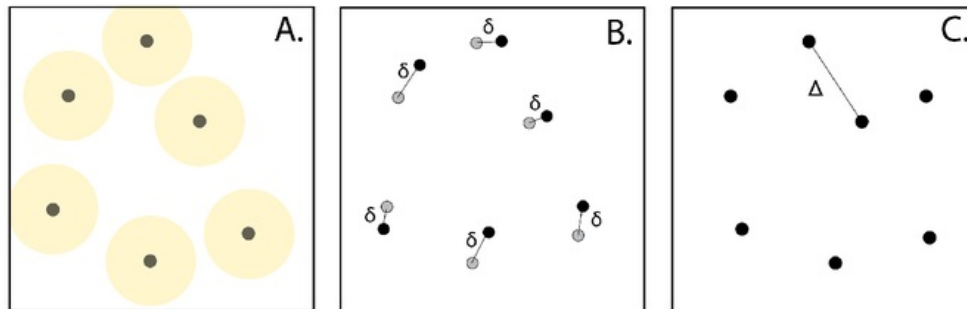


Figure 2.14: A. Illustrates the expected displacement radius for a set of detected particles. B. Illustrates the linking of particles inside the expected displacement radius. C. Defines the particle separation as Δ

Chapter 3

Microfluidic Device Fabrication

The first aim of this thesis was to develop a microfluidic device for the characterisation and separation of NDs. The processes of photolithography and soft lithography were used in the fabrication of optically accessible, microfluidic devices. This chapter outlines the design and process of fabrication before reviewing the devices performance as a product of design decisions. Section 3.1 outlines the requirements of the microfluidic device. Section 3.2 reviews the design that was selected for this application. Section 3.3 outlines the methods of photolithography, soft lithography and assembly that were used. Section 3.4 summarises the chapter.

3.1 Design of the Microfluidic Device

The device was designed with considerations of time, cost and functionality. The functionality of the device governed the features of the channel and the devices construction. The processes of photolithography and soft lithography were selected for the fabrication as the resulting devices are cheap and easy to fabricate. This section outlines the design of the channel, the fabrication process and material construction of the devices.

Requirements and Considerations

The design of the microfluidic devices had a number of requirements to fulfil. The functional requirements of the device included an ability to receive and move suspended particles through the channel while maintaining laser accessibility and particle observability. The fabrication process needed to be reliable and repeatable. The materials used to construct the device were selected as they are relatively cheap and easy to fabricate.

Channel Features

This thesis used a device with multiple inlet/outlet plugs that were connected to an offset channel via tubing. The device was mirrored across a set of elongated pillars that dissected the channel length. The channel was offset from the plugs to push the fluid flow to the edge of the microfluidic device, in an attempt to improve the optical accessibility of the devices channel. The channel features a grid of pillars that support the roof to prevent sagging (sagging often occurs when a channels width is significantly larger than its height). The photomask used to define the channel is shown in figure 3.1 and the dimensions of the channel are listed in table 3.1.



Figure 3.1: Schematic of the photolithographic mask that was used in the fabrication of the channel. This mask is transparent in the white areas and opaque in the black areas. The device features inlet/outlet plugs, connecting tubing and a pillared channel. The device is designed to be treated with an inlet and outlet end. The fluid flows into one pair of inlets along the channel length before flowing out of a pair of outlets.

Table 3.1: Dimensions of the Channel

Feature	Size
Diameter of the Inlet/ Outlet plugs	2 mm
Length of the Channel	36 mm
Diameter of the connecting tubing	40 μm
Pillar Width	40 μm
Width of the Channel	520 μm

Fabrication Overview

Photolithography: created a plug of the channel.

Soft lithography: cast a mold of the channel, embedding the features in a PDMS peel.

Cut/ Punch: the PDMS peel was cut to size and punched to enable fluid intake.

Assembled: the cut PDMS peel was then plasma bonded to a cover glass slide.

Additional Soft Lithography: added an optical window to the channel side of the assembled device.

Device Construction

The device was fabricated using PDMS, SU-8 and cover glass slides as these products allow for the quick development of cheap devices. SU-8 photoresist was used to create a plug of the channel structures on a flat surface. SU-8 was used as it is a negative photoresist with a high fidelity. A PDMS peel was cast on the SU-8 structures to embed the elastomer with the features of the channel. PDMS was used as the transparency of the material enabled laser permeation. The PDMS peel was plasma bonded to a cover glass slide to allow fluid to flow through the channel of the PDMS - Glass boundary. The reduced depth of the cover glass ensured channel observability. Additional PDMS was applied to the side of the device to create an optical window. The PDMS formed a perpendicular surface that was designed to enable laser propagation inside the device. An illustration of the assembled device is shown in figure 3.2.

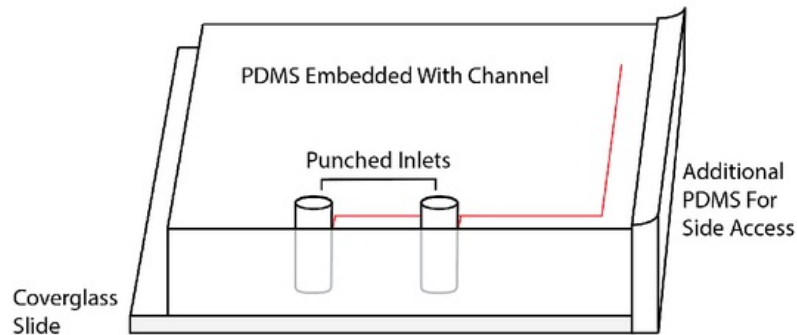


Figure 3.2: The devices of this thesis used half of the channel, allowing 2 devices to be fabricated from a single PDMS peel. The device was assembled with the embedded PDMS bonded to a cover glass slide. The device was then reoriented to apply additional PDMS and enable optical access along the channel edge.

3.2 Process of Fabrication

Photolithography and soft lithography are processes of microfabrication that create reusable microfluidic devices that enable the manipulation and observation of suspended nanomaterials. This section reviews the methods of photolithography and soft lithography that were performed in the clean room of E7B-338. A detailed explanation of the procedures is essential as it allows for both an evaluation and replication of the results.

3.2.1 Photolithography

The following photolithographic recipe was used to create 6 μm structures from SU-8 GM1060 photoresist. The recipe used information from the photoresist's data sheet to tailor the process to the specifications of the Macquarie University laboratory.

Step 1. Substrate Preparation

The substrate was prepared by cleaning organic materials from the surface of the silicon wafer. In E7B-338, the March PX-250 Plasma System was used to perform an oxygen based clean using the settings outlined in table 3.2.

Table 3.2: Plasma Settings for Cleaning

Setting	Value
Pressure	430 mTorr
Power	200 watts
Time	300 seconds

Step 2. Spin Coat

Spin coating was used to evenly distribute the photoresist onto the silicon substrate. The Macquarie University clean room uses a Laurell WS-400BZ-6NPP-Lite Spin Coater with 2 steps to distribute a 1-inch pool of the SU-8 GM1060 photoresist. The first step defined the acceleration ramp, it was set at 4120 rpm/s² over 4 seconds. The second step defined the extended spin speed, it was set at 4120 rpm/s for a period of 40 seconds.

Step 3. Soft Bake

Soft baking was used to release solvents from the photoresist. The soft bake had a temperature ramp of 4°C/min from a starting temperature of 65°C to a target temperature of 95°C. The wafer was removed upon reaching the target temperature to preserve the photosensitivity of the SU-8 layer.

Step 4. UV Exposure

Exposure of the photoresist to UV radiation initiates the cross linking (hardening) of the exposed regions. This thesis used a repaired Karl Suss MJB3 200W Mask Aligner for this exposure. The mask aligner mounts a photomask between the soft baked SU-8 and UV LED array. This process used an exposure dose of 10 mW/cm^2 for 55 seconds.

Step 5. Rest

The exposed wafer is rested for 10 minutes. This delay improves the cross linking and polymerisation over the exposed regions.

Step 6. Post Bake

Post baking was used to harden the SU-8 structures. The hotplate was set at a starting temperature of 65°C and ramped to increase the temperature at 2°C/min to the target temperature of 95°C . The wafer was left at the target temperature of 95°C for 5 minutes.

Step 7. Rest

Rest the wafer in a protected area and allow the temperature of the device to decrease.

Step 8. Develop

To develop the exposed wafer required the preparation of 3 crystallising dishes where a small amount of SU-8 developer is placed in the second dish to create a bath (figure 3.3). In the first dish, the wafer was rinsed with reusable SU-8 developer for 50 seconds. The wafer was then placed in the bath of the second dish for 10 seconds. The developed wafer was then placed over the third dish and rinsed with isopropanol to remove the developer (rinsed until the white streaks stop appearing). Leave the wafer in a protected area to dry.

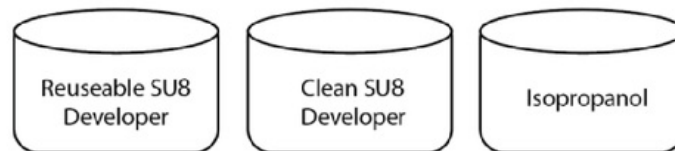


Figure 3.3: The 3 crystallising dishes used to develop the SU-8 structures of the exposed wafer. The first dish (left) was used to catch the run off of the SU-8 developer, the second dish was used as a clean bath of SU-8 developer and the third dish (right) was used to catch the run off of the rinsing isopropanol.

3.2.2 Soft Lithography

Soft lithography was used to create a mould of the SU-8 structures. The efficiency of soft lithography application and removal enabled the the creation of multiple moulds from a single wafer. The following recipe was used to create and set a PDMS peel.

Step 1: PDMS Preparation

The PDMS base and curing agent are used in a 10:1 ratio (3 g of the base and 0.3 g of the curing agent covered a single channel with PDMS). The PDMS parts were mixed together (this mixing introduced bubbles). The mixture was placed inside a desiccator and degassed at -1 atmosphere for 10 minutes.

Step 2: PDMS Pour and Exposure

The degassed PDMS mixture was poured over the SU8 structures of the silicon wafer. The PDMS covered wafer was placed in an oven and exposed to 65°C for a 2 hour period.

Step 3: PDMS Peel and modification

After exposure the set PDMS was peeled from the wafer. The peel channel side down on a clean/ flat surface. A sharp blade is used to cut the peel and a biopsy punch creates holes at the inlet plugs. We cut the device in half (across the channel width) to create 2 devices from a single peel.

Step 4: Plasma bonding the PDMS Peel

The PDMS peel was plasma bonded with the cover glass slide using the March PX-250 Plasma System. The system exposes the surfaces using the settings of table 3.3. The mask aligner was used to align the bonding. The cover glass slide was placed on the wafer plate of the Karl Suss unit and the non-channel side of the PDMS peel was attached to a transparency sheet that was fastened to the mask holder. The two surfaces were pressed together and the resulting device was placed in an oven for a 1 hour exposure at 65°C.

Table 3.3: Plasma Settings for Bonding

Setting	Value
Pressure	300 mTorr
Power	10 watts
Time	22 seconds

3.2.3 Fabrication of an Optical Window

The application of additional PDMS to the channel side of the device, created a flat surface that enabled laser propagation inside the channel. The modification of the assembled device to create an optical window was an important fabrication step towards the completion of the laser experiment.

Step 1. Removal of Excess PDMS

To reduce the distance to the channel, the excess PDMS was removed from the channel edge. The assembled device was placed PDMS side down and a blade was used to cut the PDMS along the cover glass edge (figure 3.4).

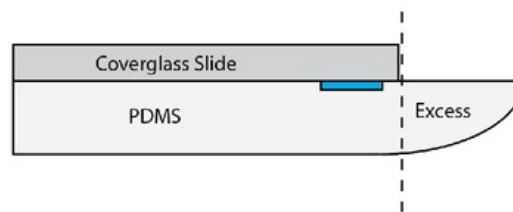


Figure 3.4: The excess PDMS was removed using a blade to along the edge of the cover glass (dotted line).

Step 2. Stand the microfluidic Device and Pour PDMS

The PDMS side of the device was mounted on a glass slide (using the stickiness of the PDMS). A bulldog clip was attached to the slide to hold the device in the position illustrated by figure 3.5. A 1 cm pool of PDMS was placed at the end of the device and the setup was placed in a 65°C oven for 2 hours. After the additional PDMS had set, the device was removed from the glass slide. This method for optical access appears successful in figure 3.6, as an undistorted image of the cross section is captured.

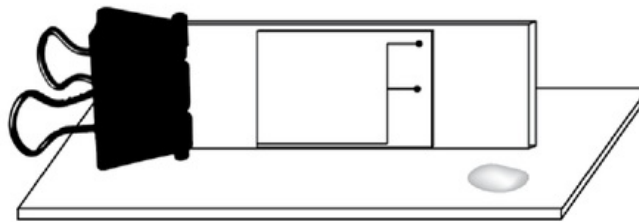


Figure 3.5: A bulldog clip holds the device and slide at a perpendicular to the base surface. This configuration is used to set the PDMS of the optical window inside the oven.

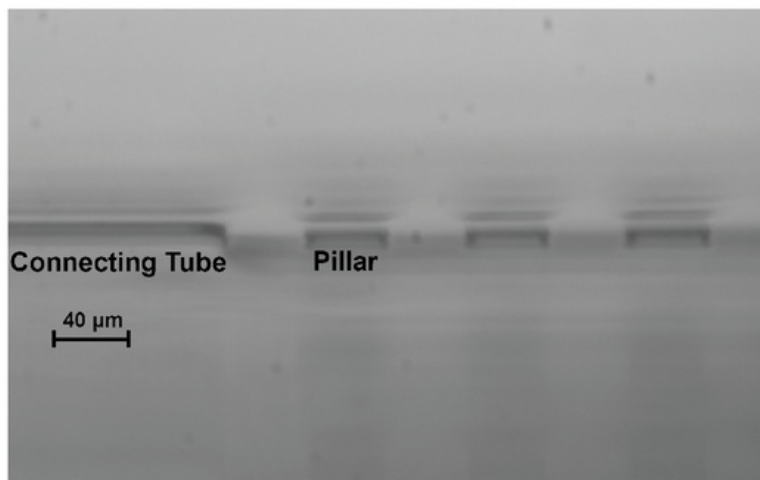


Figure 3.6: Image of the microfluidic channel with optical side access, taken through the side access to capture the cross section of the 6 μm channel.

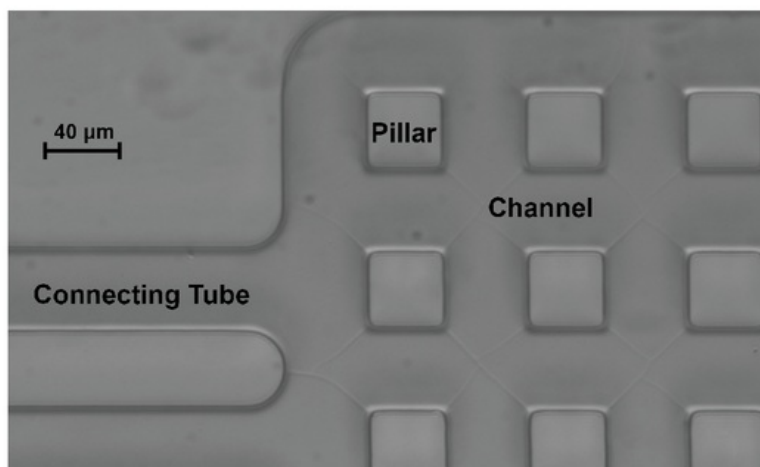


Figure 3.7: Image of the microfluidic channel with optical side access shows the top view of the same portion of the device.

3.3 Process Revisions

The fabrication process was refined to improve the resulting microfluidic devices. Revision of the process of photolithography optimised the SU-8 structures. This section outlines the channel height reduction and exposure optimisation of this thesis.

3.3.1 Channel Height Reduction

The use of particle tracking to analyse the videos, introduced a need for focused images of extended particle trajectories. This requirement was a problem in a tall channel as vertical diffusion resulted in particles travelling across the microscopes depth of field. This was an enduring constraint as the use of high powered objectives reduces the depth of field of the microscopes configuration.

To extend the observation window of the channel, the channel height was decreased from $30\text{ }\mu\text{m}$ to $6\text{ }\mu\text{m}$. To reduce the channel height, the acceleration step was increased from 1080 rpm/s^2 over 6 seconds to 4120 rpm/s^2 over 4 seconds and the extended spin speed was increased from 1080 rpm/s for a period of 60 seconds to 4120 rpm/s for a period of 40 seconds.

The resulting change in channel height had visible improvements in image quality (figure 3.6A is an image of the $30\text{ }\mu\text{m}$ channel and figure 3.6B is an image of the $6\text{ }\mu\text{m}$).

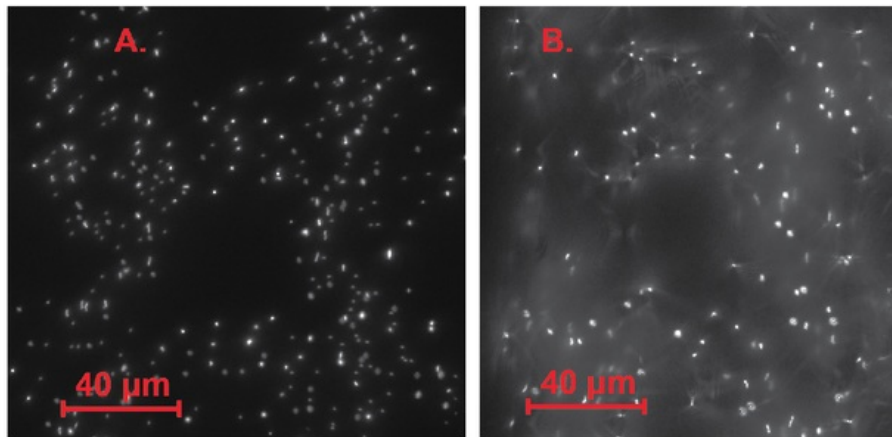


Figure 3.8: A. (left) Image of the $6\text{ }\mu\text{m}$ channel produces a focused image with a clear contrast between the uniform particles and the channel features. B. (right) Image of the $30\text{ }\mu\text{m}$ channel produces a clouded image with extreme difference in the size and intensity of the recorded particles.

3.3.2 UV Exposure Dosage

This thesis used an exposure dose matrix to optimise the length of exposure for 6 μm structures. The exposure of a single wafer was sectioned into 600, 500 and 400 second exposure lengths. The structures of the SU8 chip were then compared with the feature sizes on the original mask using bright field microscopy images. The mask and SU8 structures were compared using feature size and feature separation, where the pixel difference between the 2 images were compared numerically. This quantification of error against exposure length was calculated from multiple measurements of the same image. The resulting error was then averaged and plotted against exposure length (figure 3.8).

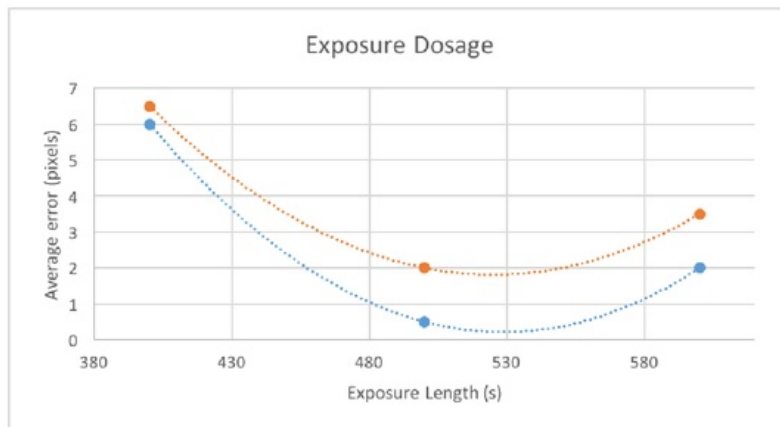


Figure 3.9: Exposure lengths plotted against the accuracy of the resulting SU8 structures. The red line highlights the average error of feature size against the length of exposure. The blue line plots the average error of feature separation against the length of exposure.

The resulting curve exhibited a parabolic shape, the average pixel error of both curves was minimised at an exposure length of 530 seconds. Therefore, the 400 and 500 second exposures represented an underexposure and the 600 second exposure represented an overexposure.

The UV exposure dosages required further refinement after week 6 as the Karl Suss mask aligner was repaired. A new LED array was installed for the emission of UV radiation. This array was tested following concern about the relative strength of the UV lamp over time. This test was conducted by placing the probe of the UV radiation meter at the height of the silicon wafer during an extended exposure (table 3.4 UV lamp intensity over time).

Table 3.4: UV Lamp intensity over time

UV Lamp Performance	
Time (min)	UV lamp Intensity (mW/cm ²)
1	0.1
2	0.1
3	0.1
4	0.1
5	0.1
6	0.1

The result of this experiment was a constant UV radiation intensity equal to 0.1 mW/cm². This result quelled concerns related to fluctuations in strength and the non-linearity of exposure doses. A linear exposure dose is critical in controlling the exposure of the photolithographic processes.

3.4 Chapter Summary

In this chapter, the design of the microfluidic device was reviewed. This revision covered the requirement of the devices, the channel features, the process of fabrication and the material construction of the device. The device was designed to pass a solution of nanomaterials while ensuring observability and laser accessibility.

The chapter then discussed the process of fabrication, discussing the photolithography of the structures, the soft lithography of the mould, the assembly of the parts and the creation of an optical window on the side of the device. This section created a reliable procedure for the creation of the designed device.

The chapter concluded with a revision of the process of photolithography, this revision focused on the channel height and exposure length that was used in this thesis. These revisions were used to optimise the features of the channel.

Fabrication of an optically observable and accessible microfluidic device initiated the organisation of the laser experiment. At this point laser training and eye tests were completed to streamline the CSIRO laser experiment. Multiple microfluidic devices were created from the recipes of this chapter for implementation in the configuration of the laser experiment.

Chapter 4

CSIRO Laser experiment

Dr. Thomas Volz, Mathieu L. Juan and Carlo Bradac established the optical setup at the CSIRO Lindfield site to utilise a high powered laser. This team of quantum physicists have an instrumental understanding of nanomaterials and optical physics [6]. Before the optical experiment could be completed an external eye tests and a laser induction were completed to ensure safe conduct and project liability. This chapter outlines the aims of the experiment before reviewing the configuration and the video output of the experiment. Section 4.1 outlines the optical configuration, section 4.2 describes the optical components, section 4.3 defines the microscopes configuration, section 4.4 describes the microscopes components, section 4.6 reviews the resulting microscopic images and section 4.7 discusses the results of the laser experiment.

Aims of the Experiment

The primary aim of the laser experiment was to gain video footage of nanomaterials experiencing controlled scattering forces. This aim required the observation of:

- Nanomaterials diffusing within the microfluidic channel;
- Laser propagation inside the channel (to validate the devices optical accessibility);
- Varying scattering forces impacting the movements of suspended nanomaterials.

Considerations

The Optical Configuration was setup to send a focused Gaussian beam into the channel of the microfluidic device. The microscope configuration was designed to observe the channel using bright field and dark field microscopy. Titania particles were used to increase the scattering force effect, in response to the large radius (475 nm) and high refractive index (2.6142) of the titania particles.

Process of the Experiment

1. Create a 100x dilution of titania particles in deionised water;
2. Wet the channel of the microfluidic device with the titania solution;
3. Mount the microfluidic device to the Piezo stage;
4. Impact the channel of the device with different laser powers (10 mW and 70 mW);
5. Observe the particles in the channel and record the video output of the microscope.

4.1 Optical Configuration

The optical configuration adapted an optical trap, to direct a focused laser towards the channel of a microfluidic device (mounted above a microscope objective). The previous applications of the laser table, increased the complexity of the setup as additional mirrors were required to pass previously installed components.

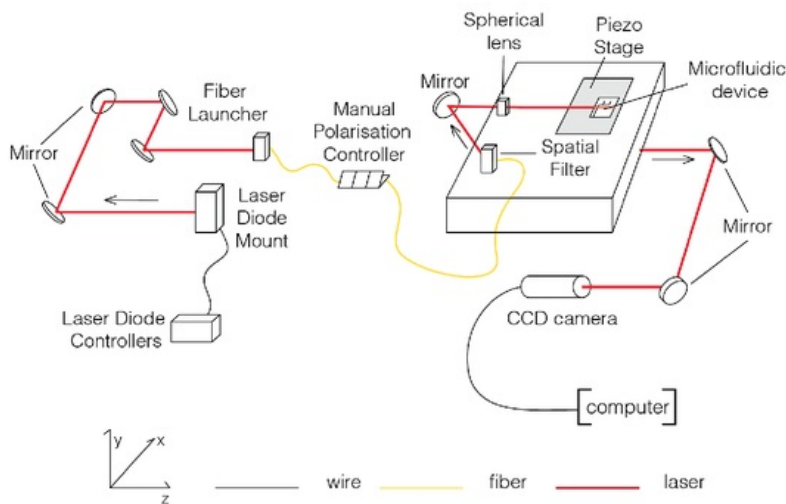


Figure 4.1: The setup was installed on an optical table that featured a grid of tapped holes that eased component installation. The optical system started at the Laser diode controllers that defined the behaviour of the laser diode. The mounted laser diode emitted a laser onto 4 mirrors before being captured by a fibre launcher. Fibre transmitted the light through a manual polarisation controller. A spatial filter re-emitted the light from the fibre as a Gaussian beam. The Gaussian beam was then reflected towards a spherical lens that focused the laser to a point inside the channel of the microfluidic device. The resulting image was input to the computer via a CCD camera. A schematic of the microscope setup is provided in figure 4.2 with a description of the microscopes configuration and components provided in sections 4.5 and 4.6.

4.2 Components of the optical setup

This section breaks down the lasers path into interactions with components. This section focuses on the experiments optical elements, while sections 4.5 and 4.6 focus on the elements of the microscope. The optical configuration creates a path of laser light that is polarised using fibre elements before being re-emitted and focused as a Gaussian beam. This section outlines the function of each component.

Laser Diode Controllers

The temperature controller and current controller of a laser diode ensure the performance of the system is safe and stable. These are the first elements of the optical setup as they control the performance of the laser. The TED200C temperature controller is designed to remove heat from the laser diode via the Peltier effect [38]. The LDC205C current controller defines the performance of the laser diode as it powers the laser using a current source. The system uses a control system to modulate the current based on a user defined input [38]. Both controllers are powered by a wall outlet and attached to the diode mount via DB9 ports.

Laser Diode Mount and Diode

The TCLDM9 laser diode mount houses cooling elements that follow the directions of the TED200C temperature controller to stabilise the system. The diode mount has built in protective circuit elements that enable the extended operation of the laser without a variation in power, wavelength or performance. The diode mount houses cooling elements that follow the directions of the temperature controller. The mount houses the diode in a socket that fasten using a clamp ring [38]. The diode mount can output light with a range of wavelengths and powers. The laser diode uses photon interactions over internal cladding to crowd and amplify the light intensity [12]. The resulting light is propagated from the top of the diode as a free-space laser (travelling parallel to the table).

Fibre Elements

Fibre is used to transport the laser using the concept of TIR. The use of fibre enables an irregular path and the implementation of polarisation controls. The optical setup uses a fibre launch system to pass the light through a manual polarisation controller before emitting the laser as a Gaussian beam from the spatial filter.

The KT110 fibre launch system focuses the free-space laser within the fibre optic cable. The launch system serves to collimate and focus the laser to enable the light to travel within the fibre [38]. This system achieves an efficient laser transmittance by matching the incident field distribution to the mode of the fibre [29].

The FPC030 is a manual polarisation controller that manually polarises the light travelling within the fibre cable using stress induced birefringence, polarising the output light with the orientation of each plate [38].

The KT310 spatial filter emits a Gaussian beam from the end of the fibre optic cable. This device converts the transmitted light back into a free-space laser by focusing the light through a pinhole and collimating the light [38].

Mirrors and a Cylindrical Lens

The laser setup utilised high quality optical mirrors to change the direction of propagation using reflection. The mirrors were controlled using mounts that rotated about the x and z axis of figure 4.1. A spherical lens was installed before the device to focus the laser light to a point inside the channel of the device.

4.3 Microscope Configuration

The microscope was configured to observe the channel using bright field and dark field microscopy. The camera captures the reflected output of the microscopes observation, transferring a sequence of images to the computer. This section reviews the configuration of the microscope (figure 4.2).

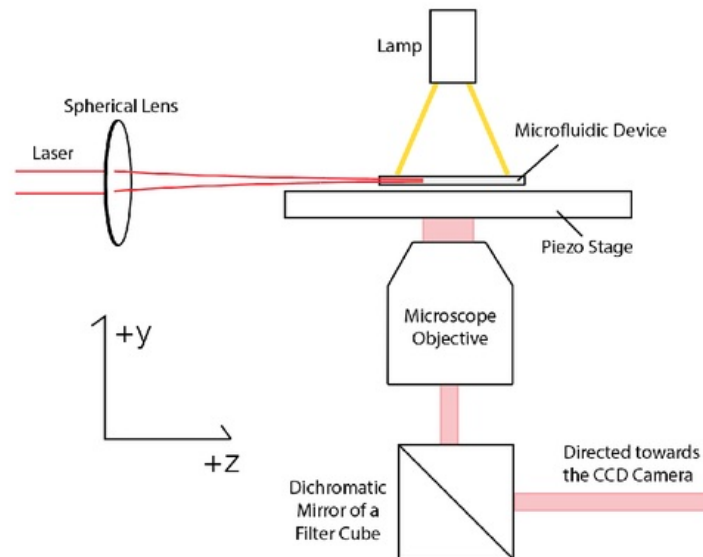


Figure 4.2: The microscope placed an objective beneath the channel of the microfluidic device. The image produced by the objective was reflected by the filter cube towards a pair of mirrors (figure 4.1). These mirrors passed the image towards the lens of a computer connected CCD camera. The bright field setup illuminated the device with a halogen lamp (mounted above the stage). To perform dark field microscopy, the lamp was disconnected and the light that scattered off disturbances was captured by the objective.

4.4 Components of the microscope setup

Halogen Lamp

The halogen lamp was positioned above the microfluidic device. This lamp was used to illuminate the surface of the device during bright field microscopy with the resulting image featuring dark elements on a bright background.

Piezo Stage and Objective Mount

The piezo stage (P-563.3CD) was used for small, precise, multi axis adjustments of the devices orientation. The stage introduced a system limitation as the horizontal orientation had a load capacity of 50 N. The objective mount of the microscope controlled the placement of the objective, focusing the output image.

Digital Imaging Objective

The Olympus UPLSAPO Super Apochromat objective was used to capture both bright field and dark field images. This objective is commonly used for digital imaging in optical setups as it produces robust images.

Table 4.1: Specifications of the microscopes objective

Specifications	
Name	UPLSAPO60XW
Magnification	60x
Numerical aperture	1.2
Working Distance	0.28 mm
Field Number	26.5

Lens and Camera

The CCD camera (DCU223) was equipped with a 150 mm lens to observe the image produced by the microscopes objective. The magnified image that the camera captured was input to the computers to view the channel and record a sequence of images.

4.5 Video Results

This experiment output images of bright field and dark field microscopy. The images show the titania diffusing through the channel with a drift caused by the capillary effect. The path of the laser is captured as white specks on the right side of the dark field images (a result of the laser scattering along this path).

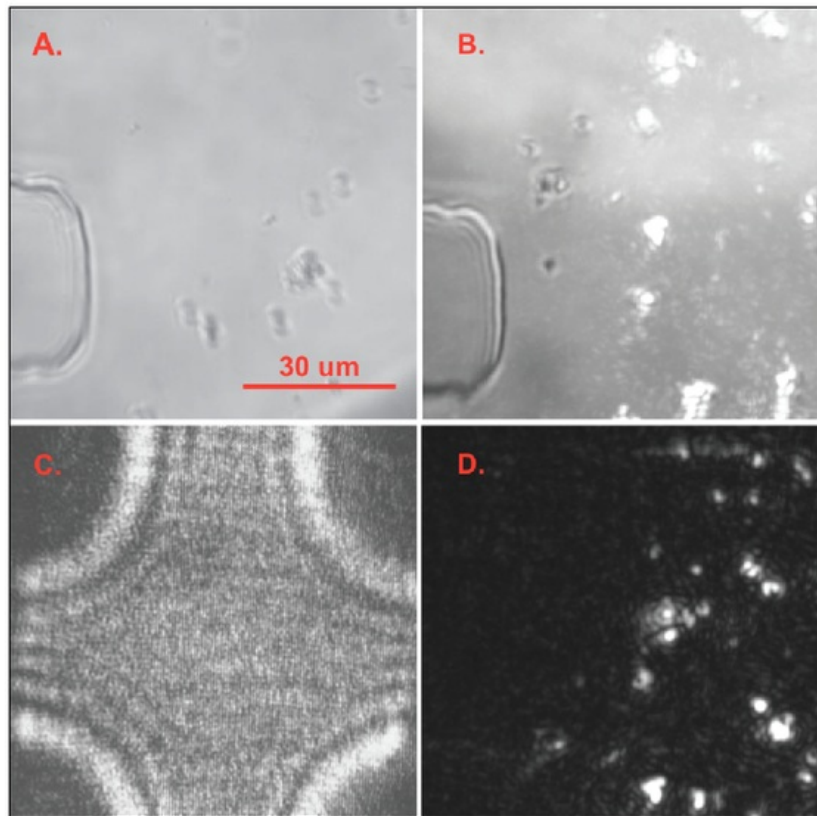


Figure 4.3: A (top left) a bright field image of the channel under a high laser power, stuck particles and a single pillar are observable. B (top right) an image that combines the outputs of bright field and dark field microscopy to overlay the path of the laser onto a bright field image of the channel. C (bottom left) a dark field image that was taken with a low powered objective. D (bottom right) an image of dark field microscopy using a high powered objective.

4.6 Process Revisions

The laser experiment exposed necessary revisions for the microfluidic device, these included considerations for the processes of fabrication, transportation, device mounting and channel wetting. This section outlines the shortfalls that were encountered along with a proposed solution to the undesired occurrences.

4.6.1 Fluid Intake and diffusion

The devices ability to receive and transport fluids was limited by the delay from fabrication to use. This effect resulted from the reduced capillary action of drier connecting tubes. The result of a reduced capillary action is in an inability to fill the channel due to a reduced intake of fluid at the inlet plugs. This limitation was overcome with labour intensive methods for forcing fluid through the connecting tubes and into the channel of the device.

To resolve this aversion to fluid intake, future experiments should wet the devices post fabrication and transport the devices submerged. The process for wetting a microfluidic device requires a desiccator and deionised water. The devices are submerged in deionised water and exposed to a vacuum of -1 atmosphere for 10 minutes (removing gas from the devices channels). After the vacuum is released, the water wets the device by filling the gaps that were previously filled with gas. The device should remain submerged for transportation to ensure that the channel remains wet. This process of wetting the channel ensures that the device continues to accept fluids [30]

4.6.2 Device Mount

Restrictions in the microscope setup coupled with the shallow height of the laser propagation relative to the piezo stage introduced a mounting issue. The devices were placed on a cantilever to position them over the observation window. This cantilevering enabled the objective to observe the channel despite its restricted travel. To resolve this for future implementations of the optical setup, a mounting mechanism should be designed and mounted to the Piezo stage.

4.7 Discussion of the Laser Experiment

The high power of the laser introduced the need for Mathieu Juan and Carlo Bradac to conduct the experiment. Dr. David Inglis also attended the laser experiment to streamline the microfluidic implementation. The presence of skilled professionals for the laser experiment produced a video output of titania diffusing in an optically impacted channel. This section reviews the resulting video output to identify limitations with recommendations to improve the results of future experiments.

The simplicity of the microscopes configuration introduced an ease of operation and adaptability to apply different microscopy techniques. However, the images of diffusing beads were poorly focused. Future configurations should be more robust and capable of producing a focused image of the diffusing beads.

The optical table created an ease of installation and recognisable reference planes. However, the table introduced a large amount of vibration as fixed features such as the pillars can be observed bouncing between the frames of the video. This vibration should be considered a result of interactions between the users and the table. Future experiments should aim to limit these vibrations by reducing table interactions or improving the stability of the optical table.

The video output of the laser experiment was limited to a short period of observation (the 4 videos resulted in 2.75 minutes of footage). This limited the videos to the observation of an insufficient number of particles. Future experiments should extend the duration of observation to collect a complete sample.

4.8 Chapter Summary

This chapter reviewed the CSIRO laser experiment. This was an important stage for this thesis as it recorded the impact of a high powered laser on suspended particles. The configurations and components of the laser experiment were reviewed to understand the function of the system and the video results were examined to assess the effectiveness of the experiment.

The configuration set up by the Volz group, struggled with the observation of the channel as the microscope was configured with a limited vertical travel that introduced mounting difficulties. The direction of the lasers path was also limited by the configuration as a single mirror mount controlled the path of the laser into the microfluidic device.

The results and discussion section focused on the output of the video footage with revisions for future experiments.

Chapter 5

Processing and Analysis of Laser Experiment

This analysis for the laser experiment modelled approximations of optical forces to the particle tracking output. The approximations used experimental parameters to define the forces acting on the particles. The particle tracking codes used image sequences to map the trajectory of each particle. This chapter is sectioned into a theoretical analysis (5.1), an experimental analysis (5.2) and a discussion of the relative results (5.3).

Aims of the Analysis

The primary aim of this analysis is to calculate the expected optical forces and compare those values to what was observed experimentally. This aim requires that we make a number of approximations (5.1.1) to calculate a force on each particle and that we experimentally track the motion of particles to calculate an experiment based force.

5.1 Theoretical Analysis

This section targets the first aim of the analysis. The design and variables of the laser experiment completed in chapter 4 are in the calculation of a theoretical approximation. The hypothesis and assumptions of 5.1.1 outline the expected system behaviour. 5.1.2 outlines the experiment based variables that were used in the force approximations. 5.1.3 calculates the scattering and gradient forces that result from different spatial coordinates. 5.1.4 determines the relative force effect for a particle in the optical setup.

5.1.1 Experimental Expectations

The expectations of the experiment were outlined to complete the process of analysis. The hypotheses guided the force calculations and the assumptions simplified the theoretical approximations to allow for a calculation of the expected force.

Hypothesis:

- The magnitude of the gradient force is expected to be small because of the long focal length of the spherical lens.
- The scattering force is expected to dominate the trajectory of the suspended particles, pushing the particles in the direction of laser propagation.
- The large particle size and high refractive index of the titania particles is expected to amplify the effect of the scattering forces.

Assumptions:

- The light passes entirely through the side window to enter the channel
- The laser is focused with a maximum intensity inside the channel.
- The Rayleigh approximation holds for Mie regime particles
- Light and particle interactions at the top and bottom of the channel are ignored.
- 100% of the transmitted power enters the channel.
- The path of the laser is considered without a diverging beam.

5.1.2 Optical Force Equations

This section follows the Harada and Asakura paper [16] to gain a theoretical expression for the optical forces acting on a dielectric sphere. The paper identifies the scattering and gradient components of the optical forces separately. This section defines the equations before calculating the theoretical forces acting on the particles of our experiment.

The scattering force is applied in the direction of propagation (z), the magnitude of this force is given by equation 2.6.

The relative refractive index: $m = 1.966$ (when $m > 1$, the gradient force is applied towards the centre of the beam waist).

The gradient forces is composed of 3 axial forces, these forces are defined by equations 2.7, 2.8 and 2.9 of this document.

5.1.3 Selected Variables of the Experiment

The optical setup at the CSIRO facility was defined by Bradac and Juan, to maximise the effect of the optical forces. The values selected by these physicists are shown in Table 5.1.

Table 5.1: Parameters of the laser experiment

Variable	Definition of the variable	Value
Output of the Laser Diode Controller	Current supplied to the diode	505.05 mA
Output of the Temperature Controller	Target temperature for the diode	33.36° C
Laser Diode (λ)	The lasers wavelength of emission	780 nm
Laser Power (P)	The measured power of the laser	10 mW & 70 mW
Fibre Polarisation	Geometrical orientation of oscillation.	$(3/8) \lambda$
Particle Radii (a)	The radius of the Titania particles	475 nm
Particle Refractive Index (n_1)	The index of refraction for Titania	2.6142
Surrounding Refractive Index (n_2)	The index of refraction for Water	1.33
Microscope Objective	Magnification / NA of Objective	60x / 1.2
Camera Frame Rate	Number of images taken per second	30 fps
Beam Waist Radii (w_0)	The beam radius at a lasers focus	40 μ m

5.1.4 Optical Force Approximation

Placing a particle at the centre of the beam waist $[0,0,0]$, results in a maximised intensity distribution for the scattering force. The maximised scattering force is represented by equation 5.1.

$$F_{scat}(r) = z \left(\frac{n_2}{c} \right) C_{scat} I(r) \times 1 \quad (5.1)$$

The optical forces at the centre of the beam waist, are approximated with a scattering component of 31.2 piconewtons along the z axis and a gradient component of 0 newtons. There is no gradient force at $[0,0,0]$, as this is the focus (point of highest intensity). Using the approximations for scattering and gradient force from the Harada paper [16], a simulation of the expected force for a set of coordinates can be calculated. The results of these calculations are shown in appendix A.2 and demonstrated in figure 5.1. This figure places a set of force vectors, at regular intervals over a dark field image of the laser experiment. The laser is focused at $[0,0,0]$ and a grid of position based vectors are generated at $5 \mu\text{m}$ intervals on the x-axis and $10 \mu\text{m}$ intervals on the z-axis. The matlab code that produced figure 5.1 is provided in appendix A.1.

5.1.5 Theoretical Particle Behaviour

The magnitude of the approximated forces are hard to observe visually. Therefore, equation 2.12 was used to convert the expected force into an expected particle velocity due to laser interaction. The resulting velocities enabled a comparison with the trajectories of the particle tracking outputs. Table 5.2 expresses the the particle velocity using a dynamic viscosity of 0.001 for water ($\mu = 0.001$).

A review of this table exposes an approximation error as the expected velocities are huge. The use of this approximation on a $100 \mu\text{m}$ particle would result in a force, capable of pushing the particles at the speed of light. The approximation error was introduced to the calculations by the large size of the titania particles. These particles broke the conditions for a Rayleigh approximation as $a > \lambda$. The breaking of this condition, led to an overestimation of the magnitude of the force.

5.2 Particle Tracking

Particle tracking was used to plot the spatial coordinates of a particle over time, this created a set of vectors for each video that mapped the particle trajectory. This analytical tool is often used in microscopic sciences to extract information about particle movements. This section outlines the particle tracking process and the particle tracking results for the laser experiment. The aim of the particle tracking is to calculate the velocity response to optical forces.

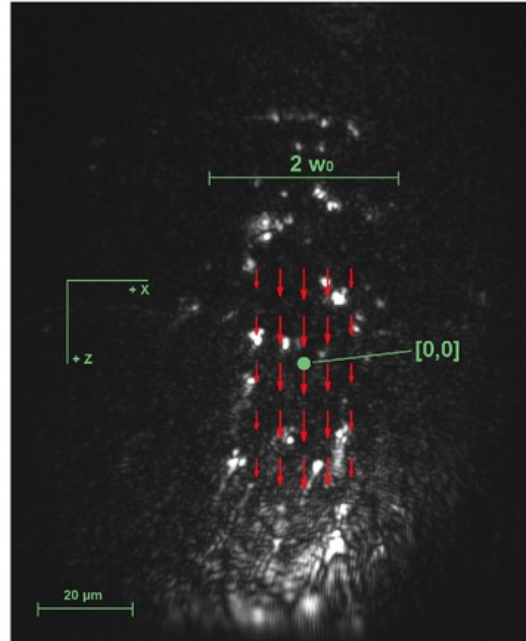


Figure 5.1: This is a dark field image of the lasers path overlaid with a vector plot of the optical forces related to a $40\text{ }\mu\text{m}$ beam waist ($2w_0$). The force vectors length corresponds with the magnitude of the force and the orientation of the vector arrow defines the direction of the force.

5.2.1 Methodology

The analysis of the experiment used Imagej to process the videos. This software decomposes a video into a sequence of images. The output of the laser experiment was processed with the mtrackj plugin. Mtrackj is a manual plugin that allows the user to identify the particle positions for each frame. Once identified the software links the particle of the same trajectory across frames.

The mtrackj plugin outputs the tracking information in a results table. We used matlab to visualise the results of this table, plotting each trajectory onto a single frame. The first plot "Particle Trajectory", linked the pixel coordinates for each particle over the video. This resulted in a plot of the different particle trajectories. The second plot "Particle Trajectory Overlaid", shifted the trajectories to a common origin. The resulting plot showed the trajectories moving away from the origin with a right to left trajectory (due to the capillary action of the system).

The Matlab code under Appendix A "Particle Tracking" was used to analyse the particle behaviour. This analysis is completed in the results section of this document (5.2.2).

Table 5.2: Expected Particle Velocity based on Optical Force Approximations.

Position Number	Velocity (m/s)	Velocity (um/s)
1	2.113E-03	2.113E+03
2	3.075E-03	3.075E+03
3	3.484E-03	3.484E+03
4	3.075E-03	3.075E+03
5	2.113E-03	2.113E+03
6	2.114E-03	2.114E+03
7	3.075E-03	3.075E+03
8	3.485E-03	3.485E+03
9	3.075E-03	3.075E+03
10	2.114E-03	2.114E+03
11	2.114E-03	2.114E+03
12	3.075E-03	3.075E+03
13	3.485E-03	3.485E+03
14	3.075E-03	3.075E+03
15	2.114E-03	2.114E+03
16	2.114E-03	2.114E+03
17	3.075E-03	3.075E+03
18	3.485E-03	3.485E+03
19	3.075E-03	3.075E+03
20	2.114E-03	2.114E+03
21	2.113E-03	2.113E+03
22	3.075E-03	3.075E+03
23	3.484E-03	3.484E+03
24	3.075E-03	3.075E+03
25	2.113E-03	2.113E+03

5.2.2 Results

To visualise the particle behaviour, the particle tracking output was plotted onto a Matlab figure. This plot was equipped with grid markings to quantify the trajectories, a visualisation of the beam path was placed on the figures to visualise the response of the particle trajectory relative to the laser. Figure 5.2 illustrates the trajectory of the particles under a low powered beam ($P_1 = 10mW$) and figure 5.3 shows the trajectory of the particles under a high powered beam ($P_2 = 70mW$).

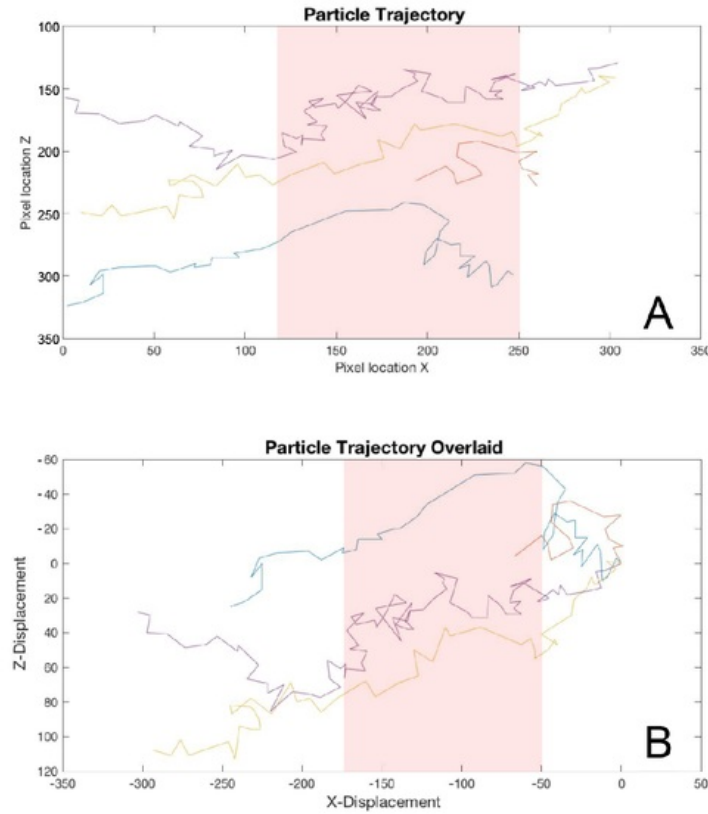


Figure 5.2: A. (top) Plots the trajectory of the particles relative to the 10 mW beam path (the pink box is equivalent to a $40\ \mu m$ beam waist). B. (bottom) Plots the trajectory of each particle under a low powered laser from a common origin. The common origin figure shows the diffusion of the particle moving right to left under the capillary action.

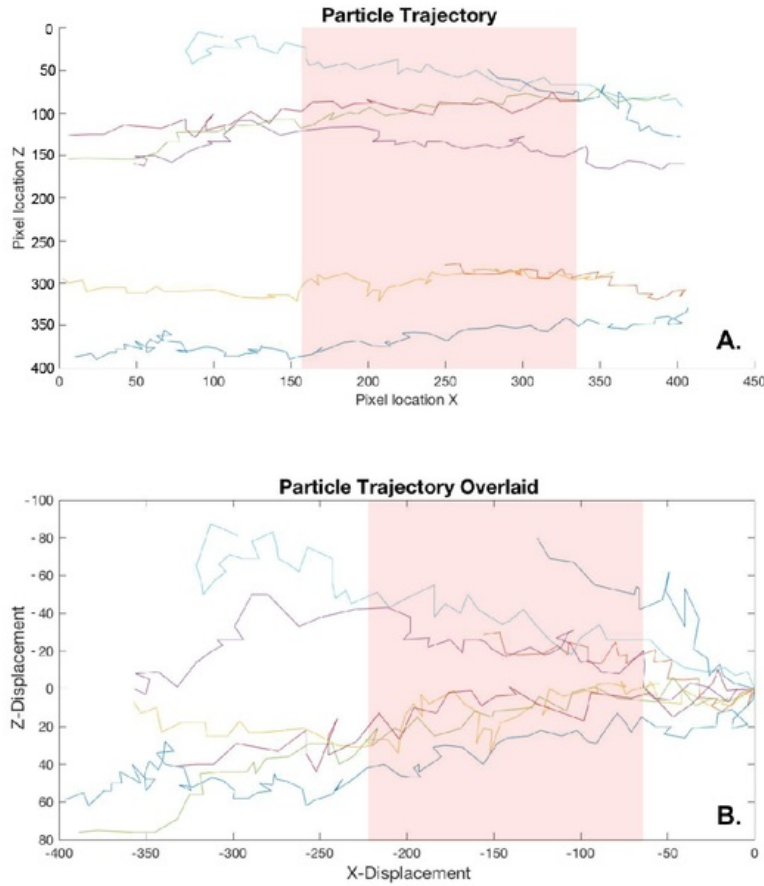


Figure 5.3: A. (top) Plots the trajectory of the particles relative to the 70 mW beam path (the pink box is equivalent to a $40\ \mu\text{m}$ beam waist). B. (bottom) Plots the trajectory of each particle under a high powered laser from a common origin. These figures capture a larger sample of particles, highlighting the right to left effect of the capillary action.

Both plots (figures 5.2 and 5.3) highlight the dominance of the capillary effect over the particles trajectory. All particles move from right to left on a trajectory that is not defined by the path of the laser. The limited number of trajectories in figure 5.1, show an overstated effect along the z axis however the magnitude of these movements should be attributed to a sampling error. These results highlight a need to reconsider the projects implementation of the laser experiment, as the current setup produces a negligible scattering force.

5.3 Discussion of Analysis

This section considers the results of the theoretical and experimental analysis, to enable an interpretation and evaluation of the larger thesis. As the two stages of analysis produce non-conforming results, this section looks for possible reasons for the deviation between the theoretical effect and effect measured using empirical data.

Revision of the theoretical analysis of the system, exposes an approximation error that was introduced to the calculations by the large particle size of the Titania. The use of these particles in the system caused a shift in system conditions from the Raleigh regime to the Mie regime. This resulted in an overestimation of the scattering force, as a result of the (a^6) relation between the radius of the particle and the resulting scattering cross section (equation 2.4).

Experimentally, the prevailing theory is that insufficient laser power was responsible for the insignificant effect of the laser. The three factors that could have impacted the strength of the laser inside the channel: were the inaccuracy in identifying the location of the focus, the conditions for TIR and the shallow height of the channel.

We believe that the shallow height of the optical access and the conditions for TIR were responsible for a significant drop off in power. Figure 5.4 highlights the inability of light to enter the channel from angles below and above the horizontal (z-axis). This was caused by the extended focal length of the spherical lens and the relative refractive index of the channel. The lens created a shallow angle for laser propagation and the refractive index of the water in the channel created the conditions required for TIR. The result of this TIR was a requirement for the laser to enter the channel through the $6\text{ }\mu\text{m}$ wall at the edge of the channel. We believe that this resulted in a 85% reduction in the effective beam waist as a $40\text{ }\mu\text{m}$ beam was reduced to a $6\text{ }\mu\text{m}$ beam.

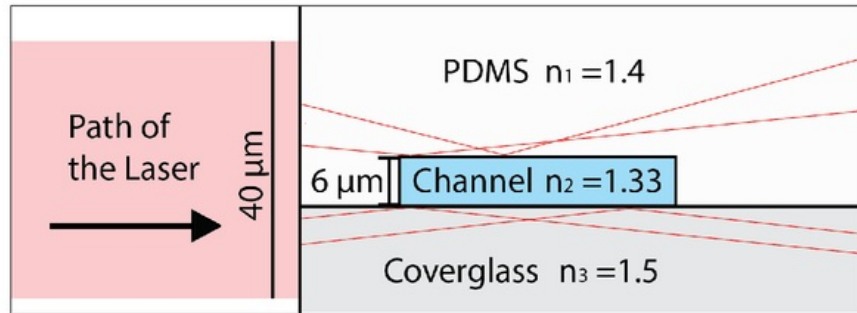


Figure 5.4: This image illustrates the significant drop off in laser power that was attributed to the shallow height of the channel and the conditions for total internal reflection. The laser travels from the left and rays that are not incident on the channel wall are reflected due to total internal reflection. This figure uses the refractive indices of each material to highlight the the conditions for TIR.

The intensity distribution and path of the laser may have also contributed to a significant drop off in laser power. The final beam path was produced with a gaussian distribution across a beam waist of $40\text{ }\mu\text{m}$. In figure 5.5, the intensity distribution of the Gaussian beam experiences a significant reduction in intensity as a result of μm displacements from the centre of the beam.

This distribution requires a significant amount of control to ensure that the focus of the laser was positioned inside the channel. The optical configuration did not have this control as the direction of the final beam path was controlled by a single mirror mount with an unmeasurable orientation. This mirror was mounted 0.3 m from the microfluidic device, that caused small variations in the orientation of the mount to have a significant impact on the focal position.

During the laser experiment, the team was unable to identify the lasers path inside the device. The method of dark field microscopy was limited to identifying the presence/absence of the laser in the channel. We believe that the lack of control for the final beam path limited this experiments ability to identify a scattering force.

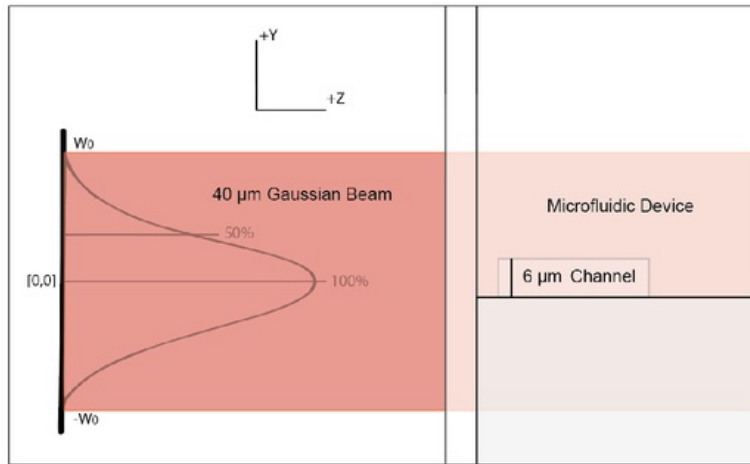


Figure 5.5: This image highlights the control requirement for the system, as the gaussian distribution shows significant drop offs in intensity away from the normal. The beam waist ($2w_0$) is equal to $40\text{ }\mu\text{m}$ and the laser propagates in the direction of positive z .

5.4 Chapter Summary

This chapter aimed to analyse the output of the CSIRO based laser experiment. This analysis had a theoretical and experimental component, that used approximation and analytical models to compare the results of the experiment to theoretical models.

The theoretical model, identified a set of force vectors that overstated the expected optical force. This was identified with the calculation of the expected velocity generating significant particle speeds. This model suffered from an approximation error as the Rayleigh assumption was broken.

The analytical model, used particle tracking of video data from the laser experiment to produce a set of particle trajectories. The particle tracking results were plotted against the laser path to enable a visualisation of the effect of the optical forces. The resulting figures did not identify a significant optical force as the particles trajectory was dominated by the capillary action.

The discussion section of this chapter, reviewed the 2 models to justify the differences in the expected force. We believe that insufficient laser power was impacting the particles in the channel due to the design of the device and the optical configuration of the laser experiment.

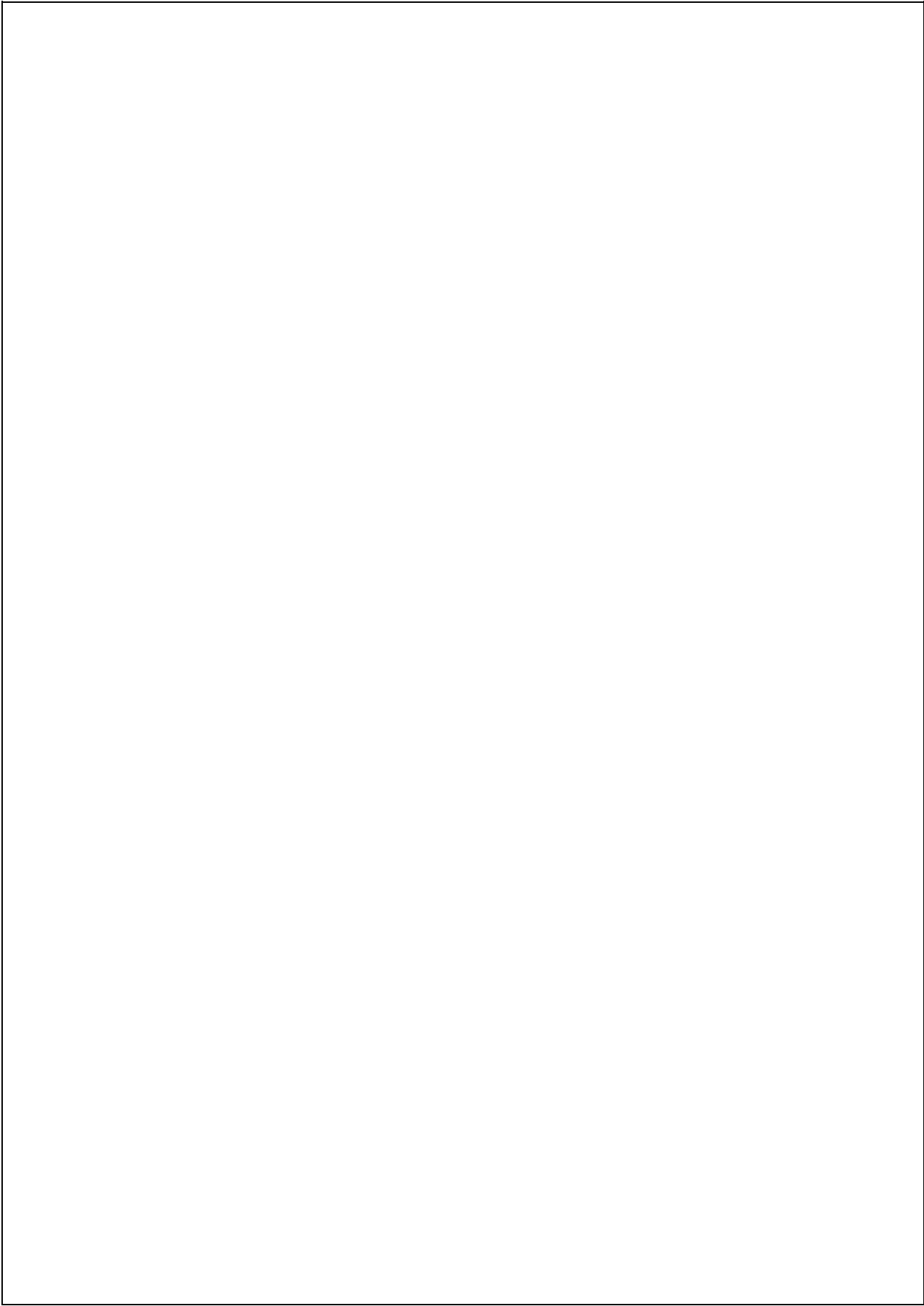
Chapter 6

Conclusions and Future Work

The aim of this project was to quantify the effect of a laser generated scattering force on suspended nanodiamonds. To achieve this goal, we developed a microfluidic device that could observe and characterise particle interactions within a channel. The microfluidic devices were filled with a particle solution and impacted by a high powered laser. This laser interaction was recorded and post processed to track the motion of each particle. This section concludes this document with a process appraisal, offering recommendations for the continuation of this research.

The background and theory section of this document contextualised the product, process and observation methods of the project. This section contained information on nanodiamonds, microfluidics, optical forces, microscopy and particle tracking. From the background and theory section, microfabrication was completed with considerations of production time, cost and process repeatability. The devices were designed to intake a particle solution and move the fluid through a pillared channel. The design ensured observability for a large magnification objective and accessibility for a high powered laser to cross the width of the channel. The fabrication of a set of identical devices enabled project collaboration at a CSIRO facility with the Volz group. This team designed an optical configuration to impact the particles in the devices channel with a high powered laser. A microscope configuration was used to record particle displacement using different microscopy techniques. After observing the particles response to external forces, the videos were analysed using particle tracking techniques. The particle trajectories were mapped and compared against the approximated forces of theoretical models. The particle tracking did not observe a particle response to the path of the laser. We believe that the devices channel height and the configuration of the laser setup caused insufficient laser power to impact the particles.

This thesis successfully produced microfluidic devices for the processing of nanoparticle solutions. However, the results of the laser experiment do not have a conclusive significance for the larger project as the small sample size and approximation errors require a reconsideration of the experiment. Continuation of this Macquarie University project requires the identification of a scattering force impacting a suspended particle solution. To improve the performance of the experiment, we conclude that future contributions to the project should focus on the optical configuration.



Consultation Meetings Attendance Form

Week	Date	Comments (if applicable)	Student's Signature	Supervisor's Signature
1	1/8	Fluorescence Microscopy	<i>j</i>	<i>Del</i>
2	8/8	Running Fluid	<i>j</i>	<i>Del</i>
3	15/8	Aligning the Band	<i>j</i>	<i>Del</i>
3	18/8	Progress Report	<i>j</i>	<i>Del</i>
4	22/8	Particle Tracking	<i>j</i>	<i>Del</i>
4	26/8	Side Access	<i>j</i>	<i>Del</i>
5	29/8	Observing Channel	<i>j</i>	<i>Del</i>
6	5/9	Simulations	<i>j</i>	<i>Del</i>
7	12/9	Laser Prep.	<i>j</i>	<i>Del</i>
Week 1	19/9	Calculation	<i>j</i>	<i>Del</i>
8	3/10	Wetting	<i>j</i>	<i>Del</i>
9	10/10	Writing	<i>j</i>	<i>Del</i>
10	17/10	Writing	<i>j</i>	<i>Del</i>
11	24/10	Forces	<i>j</i>	<i>Del</i>
12	31/10	Figures	<i>j</i>	<i>Del</i>
13	3-11	Latex	<i>j</i>	<i>Del</i>

Chapter 7

Abbreviations

ND	Nanodiamond
FND	Fluorescent Nanodiamond
NiV	Nitrogen Vacancy
SiV	Silicon Vacancy
TIR	Total Internal Reflection
PDMS	Polydimethylsiloxane
SU-8	SU-8 Photoresist

Appendix A

Calculations and Plots

A.1 Matlab

A.1.1 Matlab to generate the Vector Plot

This code was used to overlay the dark field image with a grid of vector plots using the forces and coordinates of the table A.1.

```
clc
clear
filename = '/Users/jameswhite/Documents/Workbook1.xls';
Table = readtable (filename);

scrsz = get(groot,'ScreenSize'); % Measures the screen size
figure('Name','Particle Diffusion Plots','NumberTitle','off',...
'Position',[1 scrsz(4)/2 scrsz(3)/2 scrsz(4)/2])
% Defines and positions the figure
numEntries = numel(Table(:,1)); % Counts the number of excel entries

for k=1:numEntries
    ds.k = Table.Position; % Seperates the Positions into a structure
    imshow('/Users/jameswhite/Desktop/0-95NA_device3.DF.jpg');
    %Places the DF image under the plot
    hold on

    quiver(Table.xcoord,Table.zcoord,Table.x,Table.z,...
        'linewidth',2,'color',[1 0 0]);
    %Draws Thick Red Vector Plots at specified coordinates
    title('\fontsize{14} Vector Plot');
    xlabel('x axis'),...
    ylabel('z axis (direction of laser propagation)');
    set(gca,'FontSize',14)
    hold off
end
```

A.1.2 Matlab to generate the Particle Trajectory Plots

This code was used to plot the particle trajectories that were output by the particle tracking codes, it produces to plots in a single figure. The first is a plot of the trajectories and the second is an offset plot of the trajectories using a common origin.

```

clc
clear
filename = '/Users/jameswhite/Desktop/Tracking Tables/tracking70mW.xls';
Table = readtable (filename);

scrsz = get(groot,'ScreenSize'); % Measures the screen size
figure('Name','Particle Diffusion Plots','NumberTitle','off',...
    'Position',[1 scrsz(4)/2 scrsz(3)/2 scrsz(4)])
% Defines and positions the figure

numEntries = numel(Table(:,1)); % Counts the number of excel entries

for k=1:numEntries
    ds.k = Table(Table.TID==k,:);
    % Separates the Trajectories into a structure
    M = size(ds.k,1);
    % Measures the number of entries in the structure
    ds.k(1:M,{'x','y'})
    % Takes the x,y value of the trajectory in sequence

    % Plots each particles pixel locations
    hold on
    subplot(2,1,1);
    plot(ds.k.x,ds.k.y);
    title('\fontsize{16} Particle Trajectory');
    xlabel('Pixel location X'), ylabel('Pixel location Z');
    set(gca,'FontSize',11)
    hold off

    %Overlays the origins of the first plot
    if M >= 1
        hold on
        subplot(2,1,2);
        xoffset = ds.k.x(1);
        yoffset = ds.k.y(1);
        plot(ds.k.x - xoffset, ds.k.y - yoffset);
        title('\fontsize{16} Particle Trajectory Overlaid');
        xlabel('\fontsize{14} X-Displacement'),...
        ylabel('\fontsize{14} Z-Displacement');
        set(gca,'FontSize',11)
        hold off
    end
end
end

```

A.2 Vector Calculation

This table was used by the Matlab code to generate the Vector Plot outlined in the matlab section (A.1) of this appendix.

Table A.1: Approximated Force Vectors for a 40 μm beam waist

Position Number	X coordinate (μm)	Z coordinate (μm)	Scattering Force (N)	Gradient Force in x (N)	Gradient Force in z (N)
1	-10	-20	2.09E-11	4.19E-15	-6.46E-19
2	-5	-20	3.05E-11	3.05E-15	-2.35E-19
3	0	-20	3.45E-11	0	1.91E-26
4	5	-20	3.05E-11	-3.05E-15	-2.35E-19
5	10	-20	2.09E-11	-4.19E-15	-6.46E-19
6	-10	-10	2.09E-11	4.19E-15	-3.23E-19
7	-5	-10	3.05E-11	3.05E-15	-1.17E-19
8	0	-10	3.45E-11	0	9.55E-27
9	5	-10	3.05E-11	-3.05E-15	-1.17E-19
10	10	-10	2.09E-11	-4.19E-15	-3.23E-19
11	-10	0	2.09E-11	4.19107E-15	0
12	-5	0	3.05E-11	3.05E-15	0
13	0	0	3.45E-11	0	0
14	5	0	3.05E-11	-3.05E-15	0
15	10	0	2.09E-11	-4.19E-15	0
16	-10	10	2.09E-11	4.19E-15	3.23E-19
17	-5	10	3.05E-11	3.05E-15	1.17E-19
18	0	10	3.45E-11	0	-9.56E-27
19	5	10	3.05E-11	-3.05E-15	1.17E-19
20	10	10	2.09E-11	-4.19E-15	3.23E-19
21	-10	20	2.09E-11	4.19E-15	6.46E-19
22	-5	20	3.05E-11	3.05E-15	2.35E-19
23	0	20	3.45E-11	0	-1.91E-26
24	5	20	3.05E-11	-3.05E-15	2.35E-19
25	10	20	2.09E-11	-4.19E-15	6.46E-19

Bibliography

- [1] T. M. Adams and R. A. Layton, *Introductory MEMS: Fabrication and Applications*. Boston, MA: Springer US: Boston, MA, 2010.
- [2] L. Akesso, "Gm1060 technical datasheet," p. 1–9. [Online]. Available: <http://www.gersteltec.ch/userfiles/1197841378.pdf>
- [3] A. Ashkin, J. Dziedzic, J. Bjorkholm, and S. Chu, "Observation of a single-beam gradient force optical trap for dielectric particles," *Optics letters*, vol. 11, no. 5, pp. 288–290, 1986.
- [4] A. S. Barnard, "Chapter 1 distribution, diffusion and concentration of defects in colloidal diamond," *Nanodiamond*, pp. 1–26, 2014. [Online]. Available: <http://dx.doi.org/10.1039/9781849737616-00001>
- [5] H. Berg, *Random Walks in Biology*, ser. Princeton paperbacks. Princeton University Press, 1993. [Online]. Available: <https://books.google.com.au/books?id=DjdgXGLoJY8C>
- [6] C. Bradac, M. Johnsson, M. van Breugel, B. Baragiola, R. Martin, M. L. Juan, G. Brennen, and T. Volz, "Observation of room-temperature spontaneous superradiance from single diamond nanocrystals," 2016, arXiv:1608.03119v1.
- [7] C. Bradac, M. U. D. of Physics, Astronomy, and J. R. T. s. Rabeau, "The properties of nitrogen vacancy centres in nanodiamond," 2012. [Online]. Available: <http://trove.nla.gov.au/work/181477689>
- [8] C. Bradac, J. M. Say, I. D. Rastogi, N. M. Cordina, T. Volz, and L. J. Brown, "Nano assembly of nanodiamonds by conjugation to actin filaments," *Journal of Biophotonics*, vol. 9, no. 3, p. 296–304, 2016. [Online]. Available: <http://dx.doi.org/10.1002/jbio.201500167>
- [9] G. V. Casquillas and T. Houssin., "Pdms: a review," 2008.
- [10] H. Y. Chang, Yi Renand Lee, K. Chen, C. C. Chang, D. S. Tsai, C. C. Fu, T. S. Lim, Y. K. Tzeng, C. Y. Fang, C. C. Han, H. C. Chang, and W. Fann, "Mass production and dynamic imaging of fluorescent nanodiamonds," *Nat Nano*, vol. 3, no. 5, p. 284–288, May 2008. [Online]. Available: <http://dx.doi.org/10.1038/nnano.2008.99>

- [11] P. Constantin and C. Foias, *Navier-stokes equations*. University of Chicago Press, 1988.
- [12] R. Diehl, *High-power diode lasers: fundamentals, technology, applications*. Springer Science & Business Media, 2003, vol. 78.
- [13] A. Einstein, "Invstigations on the theory. of, the brownian movement," 1956.
- [14] C. C. Fu, H. Y. Lee, C. Kowa, S. L. Tsong, H. Y. Wu, P. K. Lin, P. K. Wei, P. H. Tsao, H. C. Chang, and W. Fann, "Characterization and application of single fluorescent nanodiamonds as cellular biomarkers," *Proceedings of the National Academy of Sciences*, vol. 104, no. 3, pp. 727–732, 2007.
- [15] D. W. Hahn, "Light scattering theory," 2009.
- [16] Y. Harada and T. Asakura, "Radiation forces on a dielectric sphere in the rayleigh scattering regime," *Optics Communications*, vol. 124, pp. 529–541, feb 1996.
- [17] C. Hepp, T. Muller, V. Waselowski, J. N. Becker, B. Pingault, H. Sternschulte, D. Steinmuller Nethl, A. Gali, J. R. Maze, M. Atature, and C. Becher, "Electronic structure of the silicon vacancy color center in diamond," *Phys. Rev. Lett.*, vol. 112, p. 036405, Jan 2014. [Online]. Available: <http://link.aps.org/doi/10.1103/PhysRevLett.112.036405>
- [18] W. W. W. Hsiao, Y. Y. Hui, P. C. Tsai, and H. C. Chang, "Fluorescent nanodiamond: A versatile tool for long term cell tracking, super resolution imaging, and nanoscale temperature sensing," *Accounts of Chemical Research*, vol. 49, no. 3, p. 400–407, 2016, pMID: 26882283. [Online]. Available: <http://dx.doi.org/10.1021/acs.accounts.5b00484>
- [19] A. Jenkins, "Bioimaging: Cellular vision." *Nature Photonics*, vol. 2, no. 8, p. 464, 2008. [Online]. Available: <http://www.nature.com/nphoton/journal/v2/n8/full/nphoton.2008.141.html>
- [20] U. F. D. Johansson, A. Katrusha, P. J. K. S. Moe, and W. Wang, "Large colorless hpht synthetic diamonds from new diamond technology," *Gem and Gemology*, vol. 51, 2015. [Online]. Available: <http://www.gia.edu/gemsgemology/fall2015largecolorlesshphtgrownsyntheticgemdiamondtechnologyrussia>
- [21] S. Keller, G. Blagoi, M. Lillemose, D. Haeffiger, and A. Boisen, "Processing of thin su 8 films," *Journal of Micromechanics and Microengineering*, vol. 18, no. 12, p. 125020, 2008. [Online]. Available: <http://stacks.iop.org/09601317/18/i=12/a=125020>
- [22] T. Laurell and A. Lenshof, *Microscale Acoustofluidics*. Royal Society of Chemistry, 2014.

- [23] M. A. Lauterbach, "Finding, defining and breaking the diffraction barrier in microscopy a historical perspective," *Optical nanoscopy*, vol. 1, no. 1, p. 1, 2012.
- [24] J. C. McDonald and G. M. Whitesides, "Poly(dimethylsiloxane) as a material for fabricating microfluidic devices," *Accounts of Chemical Research*, vol. 35, no. 7, p. 491 499, 2002. [Online]. Available: <http://dx.doi.org/10.1021/ar010110q>
- [25] T. D. Merson, S. Castelletto, I. Aharonovich, A. Turbic, T. J. Kilpatrick, and A. M. Turnley, "Nanodiamonds with silicon vacancy defects for nontoxic photostable fluorescent labeling of neural precursor cells," *Opt. Lett.*, vol. 38, no. 20, p. 4170 4173, Oct 2013. [Online]. Available: <http://ol.osa.org/abstract.cfm?URI=ol38204170>
- [26] D. B. Murphy and M. W. Davidson, *Fundamentals of light microscopy and electronic imaging*. Hoboken, N.J.: Hoboken, N.J. : Wiley-Blackwell, 2013, includes bibliographical references and index.
- [27] E. Nedderman, "Stokes' law for solid spheres and spherical bubbles," 2011.
- [28] A. Neild, T. W. Ng, and W. M. S. Yip, "Optical sorting of dielectric rayleigh spherical particles with scattering and standing waves," *Opt. Express*, vol. 17, no. 7, p. 5321 5329, Mar 2009. [Online]. Available: <http://www.opticsexpress.org/abstract.cfm?URI=oe1775321>
- [29] Newport, "Filter optic basics: Tutorial," 2016.
- [30] R. S. Pawell, D. W. Inglis, T. J. Barber, and R. A. Taylor, "Manufacturing and wetting low-cost microfluidic cell separation devices," *Biomicrofluidics*, vol. 7, no. 5, p. 056501, 2013.
- [31] P. Reineck, A. Francis, A. Orth, D. W. M. Lau, R. D. V. Nixon Luke, I. D. Rastogi, W. A. W. Razali, N. M. Cordina, L. M. Parker, V. K. A. Sreenivasan, L. J. Brown, and B. C. Gibson, "Brightness and photostability of emerging red and near ir fluorescent nanomaterials for bioimaging," *Advanced Optical Materials*, vol. 4, no. 10, p. 1549 1557, 2016. [Online]. Available: <http://dx.doi.org/10.1002/adom.201600212>
- [32] L. Salasnich, *Quantum Physics of Light and Matter : A Modern Introduction to Photons, Atoms and Many Body Systems*. Cham : Springer International Publishing : Imprint: Springer, 2014.
- [33] J. M. Say, C. Bradac, C. van Vreden, C. Hill, D. Reilly, N. King, B. Herbert, L. Brown, and J. Rabeau, "Fluorescent nanodiamonds for biological applications," in *Proceedings of the International Quantum Electronics Conference and Conference on Lasers and Electro Optics Pacific Rim 2011*. Optical Society of America, 2011, p. C685. [Online]. Available: <http://www.osapublishing.org/abstract.cfm?URI=CLEOPR2011C685>

- [34] R. Schirhagl, K. Chang, M. Loretz, and C. L. Degen, "Nitrogen vacancy centers in diamond: Nanoscale sensors for physics and biology," *Annual Review of Physical Chemistry*, vol. 65, pp. 83–105, 2014.
- [35] S. Singh and S. A. Catledge, "Silicon vacancy color center photoluminescence enhancement in nanodiamond particles by isolated substitutional nitrogen on 100 surfaces," *Journal of Applied Physics*, vol. 113, no. 4, 2013. [Online]. Available: <http://scitation.aip.org/content/aip/journal/jap/113/4/10.1063/1.4783958>
- [36] D. J. Stephens and V. J. Allan, "Light microscopy techniques for live cell imaging," *Science*, vol. 300, no. 5616, p. 826, Apr 04 2003. [Online]. Available: <http://simsrad.net.ocs.mq.edu.au/login?url=http://search.proquest.com.simsrad.net.ocs.mq.edu.au/docview/213591984?accountid=12219>
- [37] L. J. Su, C. Y. Fang, Y. T. Chang, K. M. Chen, Y. C. Yu, J. H. Hsu, and H. C. Chang, "Creating high density ensembles of nitrogen vacancy centers in nitrogen rich type Ib nanodiamonds," *ArXiv e prints*, Jun. 2013. [Online]. Available: <http://adsabs.harvard.edu/abs/2013arXiv1306.1594S>
- [38] Thorlabs, "Product operation manual," 2016.
- [39] V. Vaijayanthimala, Y. K. Tzeng, H. C. Chang, and C. L. Li, "The biocompatibility of fluorescent nanodiamonds and their mechanism of cellular uptake," *Nanotechnology*, vol. 20, no. 42, 2009. [Online]. Available: <http://stacks.iop.org/09574484/20/i=42/a=425103>
- [40] I. I. Vlasov, A. A. Shiryaev, T. Rendler, S. Steinert, S. Y. Lee, D. Antonov, M. Voros, F. Jelezko, A. V. Fisenko, L. F. Semjonova, J. Biskupek, U. Kaiser, O. I. Lebedev, I. Sildos, P. R. Hemmer, V. I. Konov, A. Gali, and J. Wrachtrup, "Molecular sized fluorescent nanodiamonds," *Nat Nano*, vol. 9, no. 1, p. 54–58, Jan 2014. [Online]. Available: <http://dx.doi.org/10.1038/nnano.2013.255>
- [41] G. M. Whitesides and S. K. Y. Tang, "Fluidic optics," *Proc. SPIE*, vol. 6329, p. 63290A–63290A-13, 2006. [Online]. Available: <http://dx.doi.org/10.1117/12.681672>
- [42] C. Wurth, M. Grabolle, J. Pauli, M. Spieles, and U. Resch-Genger, "Relative and absolute determination of fluorescence quantum yields of transparent samples," *Nat. Protocols*, vol. 8, no. 8, pp. 1535–1550, Aug 2013.
- [43] J. Xiao, P. Liu, L. Li, and G. Yang, "Fluorescence origin of nanodiamonds," *The Journal of Physical Chemistry C*, vol. 119, no. 4, pp. 2239–2248, 2015. [Online]. Available: <http://dx.doi.org/10.1021/jp512188x>
- [44] J. Zhang, S. Yan, D. Yuan, G. Alici, N.-T. Nguyen, M. Ebrahimi Warkiani, and W. Li, "Fundamentals and applications of inertial microfluidics: a review," *Lab Chip*, vol. 16, pp. 10–34, 2016. [Online]. Available: <http://dx.doi.org/10.1039/C5LC01159K>